AN ABSTRACT OF THE THESIS OF

Kai Zhan for the degree of Master of Science in Physics presented on September 19th, 2014.

Title: Thermal conductivity measurements of amorphous metal thin films via the 3ω method

Abstract approved: _____

Janet Tate

Amorphous multicomponent metals have promising applications in novel electronic devices because of their atomically smooth surface morphology and lack of grain boundaries. It is important to understand the thermal transport properties of amorphous metals and an accurate measurement of their thermal conductivity will be essential for further improvement of device performance and reliability. Here, the 3ω method has been improved and extended to investigate the room temperature thermal conductivity of amorphous metals. Iterative, amorphous multicomponent metallic films are deposited on silicon substrate by magnetron sputter deposition. A thin layer of hafnium oxide film is deposited on top of amorphous metals by atomic layer deposition, providing a reliable insulation between an aluminum heater and the amorphous metal film. The room temperature thermal conductivities of thin-film hafnium oxide and silicon nitride are also measured to demonstrate the capability and reliability of the 3ω technique.

Thermal conductivity measurements of amorphous metal thin films via the 3ω method

by

Kai Zhan

A THESIS

submitted to

Oregon State University

in partial fulfillment of
the requirements for the
degree of

Master of Science

Presented September 19th, 2014
Commencement June 2015

Master of Science thesis of Kai Zhan presented on September 19th, 2014.

APPROVED:

Major Professor, representing Physics

Chair of the Department of Physics

Dean of the Graduate School

I understand that my thesis will become part of the permanent collection of Oregon State University libraries. My signature below authorizes release of my thesis to any reader upon request.

Kai Zhan, Author

ACKNOWLEDGEMENTS

I would like to sincerely thank all the people who have worked with me or helped me on this project. First I would like to thank my advisor, Dr. Janet Tate, for her continuous guidance and tremendous encouragements during the whole time of my research. Furthermore, I want to thank Dr. Tate again for being absolute supportive of my career plans. I also want to thank River Wiedle, Nicola Schmidt, whom both are former members in Tate's lab, and Mark Warner for their invaluable work in setting up the 3ω measurement system and demonstrating the capability of the system. Especially Mark Warner, with his expertise in electronics and instrumentations, helps me a lot in troubleshooting and in improving the 3ω measurement system. I also want to thank Rose Baunach and James Cutz, who also are former student work in Tate's lab, for their help in getting me familiar with the 3ω measurement. Then I want to thank John Mcglone from Dr. John Wager's group and Kris Olsen from Dr. Douglas Keszler's group for their invaluable work in the deposition of all the films to be measured. Especially John Mcglone helps me a lot regarding how to work better in Owen cleanroom and comes up with great ideas about the troubleshooting of the samples. I also want to thank the Hewlett-Packard company for proving the cleanroom at HP campus and providing the DC magnetron sputtering and atomic layer deposition tool. Great thanks to Greg Angelos from John Wager's group for helping me depositing the aluminum films using the e-beam deposition tool. Moreover, I would like to sincerely thank the Advanced Materials and Devices research group at OSU, for their contribution in creating and maintaining the Owen cleanroom. Without the help of Chris Tasker and other members that maintaining the cleanroom, this project will never be possible. Especially thanks to Rick Presley for not only training me about the photolithography and lift-off process but also lend me a hand every time I got problems about any tool in Owen cleanroom. I also want to thank Casey Hines for training me to use the Veeco thermal deposition. Thanks to Weiyang Li from Dr. Albrecht Jander's group and Fanghui Wang from Dr. Alan Wang's group, for

their help in fabricating the photolithography mask.
This project was supported by the Hewlett-Packard company.

TABLE OF CONTENTS

TABLE OF CONTENTS (Continued)

Page

LIST OF FIGURES

LIST OF FIGURES (Continued)

LIST OF FIGURES (Continued)

Figure Page

LIST OF FIGURES (Continued)

Figure Page

LIST OF FIGURES (Continued)

Figure Page

LIST OF TABLES

Chapter 1: Introduction

Amorphous metals

Amorphous metals, often known as metallic glass, refers to solid metallic materials which lacks periodic crystalline structures. The term of crystalline is used to describe materials that exhibit both short and long range order in the arrangements of atoms, while the amorphous means the long range order of atomic arrangements is missing. Amorphous metals are usually multicomponent alloys rather than pure metals and the constituent atoms are significantly different in size. Bulk metallic glass (BMG), with the absence of grain boundaries, usually has a high wear and corrosion resistance and a high resilience strength as well, and thus has a wide range of applications such as used as protective coatings for industry machinery or as scratch-free screen protector [1, 2]. Liquidmetal Technologies even have several commercially available products of titanium-based bulk metallic glass [Liquidmetal Technologies Inc, Lake Forest, CA, USA] . On the other hand, the amorphous metals often have a high resistivity because of the relatively short mean free path for electrons associated with the amorphous structures [3]. The amorphous multicomponent metal films with their atomically smooth surface morphology, lack of grain boundaries and high resistivity are promising potential candidates as electrode materials used in electronic devices, particularly in vertical-transport electronic devices such as two terminal metal-insulator-metal (MIM) tunnel diodes and three terminal hot electron transistors (HET) [3]. Since the performance and lifetime of such electronic devices are limited by the temperature and thermal transport properties of the materials, a good understanding of the thermal transport properties of amorphous metals is critically important for further improvements of the device efficiency, especially as the feature size of electronic devices keep decreasing. Thus an accurate measurement of the thermal conductivity of amorphous metals is

essential in understating their thermal properties and acting as guidance in further device performance and reliability improvements.

Hafnium oxide and silicon nitride

Hafnium oxide with the formula HfO_2 is the leading candidate to replace silicon oxide as gate oxide used in field effect transistors (FET), mainly because it has a higher dielectric constant [4]. Because of its high dielectric constant, hafnium oxide can reduce the current leakage across the dielectric even when the gate oxide is made to be ultra thin a few atoms thick [5]. The thermal properties of hafnium oxide are also increasingly important because the thermal conductivity and the thermal interface resistance can affect the phonon properties during device switching and limit the performance and reliability of such electronic devices [6, 7]. Thus an accurate measurement of thermal conductivity of hafnium oxide is also very interesting and necessary. Silicon nitride is often used as insulator to electrically isolate different structures of integrated circuits. Silicon nitride can also be used as passivation layer of microchips which acting as diffusion barrier against water molecules and sodium ions in order to avoid corrosion and instability issue in microelectronics [8]. Measuring the thermal conductivity of hafnium oxide and silicon nitride can also demonstrate the reliability and capability of our 3ω measurement system.

History of 3ω method

The 3ω method is a well-known technique used to directly measure the thermal conductivity of both bulk and thin film materials. The 3ω method was first developed by David Cahill in the late 1980s [9,10]. Cahill invented this method in order to reduce the difficulties in thermal conductivity measurements by reducing the thermal equilibration time and eliminating errors caused by blackbody radiation of the system during measurements. The 3ω method was initially demonstrated to be capable of measuring the thermal conductivity of bulk glasses. He also extended

the 3ω method to study the thermal conductivity of thin-film dielectric materials [11]. After that, the 3ω method analyzed and improved for the case of one or more thin films on a substrate of finite thickness by Kim [12] whom also show how to eliminate the effects of interfacial thermal resistance in the presence of several layer of thin films [13]. The model for the 3ω method has been carefully analyzed and simulated using the finite element method [14] and also has been extended for substrates and thick films with anisotropic thermal conductivity [15]. Over the years, the 3ω method has been extensively used in thermal conductivity measurements of a wide range of both bulk and thin-film materials. The 3ω measurement system in our lab build by River Wiedle and Mark Warner. The system has been demonstrated to be capable of measuring thermal conductivity of amorphous thin film dielectrics [16]. Here the 3ω method is extended and improved to measure the thermal conductivity of thin-film amorphous metals which have higher thermal conductivity.

Time-Domain Thermo-reflectance (TDTR) is another method to measure the thermal diffusivity of a material and the thermal conductivity as well if we know the density and the specific heat of such material [17, 18]. There is a comparison of the TDTR and 3ω method in measuring the thermal conductivity [19, 20]. The 3ω method typically has a high accuracy in thermal conductivity measurements, especially for bulk material and low thermal conductivity dielectric films. But the accuracy of the 3ω method decreases for high thermal conductivity films or conducting films. While the TDTR has a limited accuracy in thermal conductivity measurements because it depends on many experimental parameters such as the heat capacity of the sample. But the TDTR method also has several advantages: it can separate the interface thermal resistance from the total thermal resistance contributions and no electrical insulation layer is needed for thermal conductivity measurements of conducting films. In this thesis, only the 3ω method for the thermal conductivity measurements is discussed.

Structure of this thesis

The structure of this thesis is as follows. Chapter 2 presents the theoretical background for the 3ω method and a detailed derivation of the analytic solution of the heat equation that will be used to interpret the data. After that is a numerical simulation work of the 3ω method using finite element method and COMSOL. This is followed by a literature review about the thermal transportation mechanism of amorphous metals. Chapter 3 provides details about the growth and preparation of samples and the instruments used in the 3ω measurement system. New instruments aimed to improve the reliability and capability are also presented in Chapter 3. Chapter 4 shows the experimental data of the thermal conductivity measurements for amorphous metal thin films TaWSi, hafnium oxide films and silicon nitride films. Chapter 5 presents the conclusion for this thesis and suggests several prospects for the further research using the 3ω method.

Chapter 2: Theoretical background

This chapter firstly discuss the theory of the 3ω method and the derivation of the analytic solution of the heat equation used in the 3ω method. A detailed discussion of the theory of the 3ω method is critical for understanding the fundamental idea of the 3ω method. The derivation follows the format used in River Wiedle's thesis [21] and Nicola Schmidt's thesis [22]. Then a numerical approach to analysis the 3ω method based on finite element method is briefly presented. The thermal transportation mechanism of amorphous metals is also discussed in this chapter.

2.1 3ω method

The 3ω method is a well-known technique to directly measure the thermal conductivity of both bulk and thin-film materials. It was first proposed by David Cahill in the late 1980s [9]. Cahill invented the 3ω method to measure the thermal conductivity of bulk dielectric materials. The 3ω method was then extended to measure the thermal conductivity of thin-film dielectric materials [10,12]. Here we improve and extend the 3ω technique to investigate the thermal conductivity of amorphous multicomponent metallic films.

The fundamental idea of 3ω method [9,22] is to deposit a thin metal strip on the samples of interest and use the metal strip both as a heater and a thermometer. Figure 2.1 and 2.2 shows the geometry of the heater typically used in the 3ω method. A sinusoidal current $I(t) = I_0 cos(\omega t + \phi_0)$ with frequency ω and phase ϕ_0 is applied to the metal strip. It causes Joule heating at frequency 2ω inside the heater. Assuming the change of resistance of the heater is small, the generated heat power is given by:

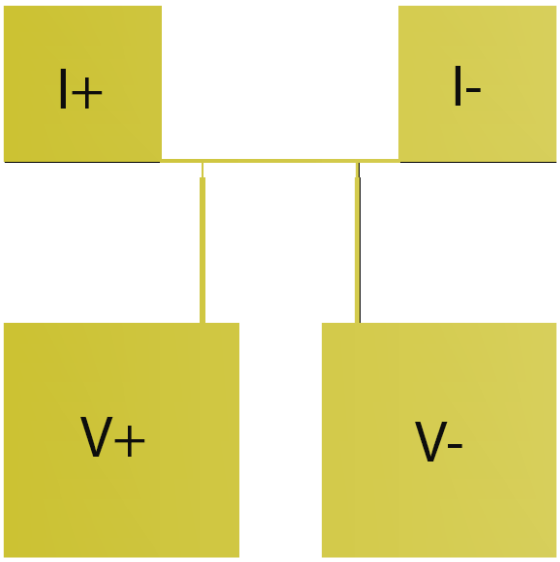

Figure 2.1: Heater structure used in 3ω method.

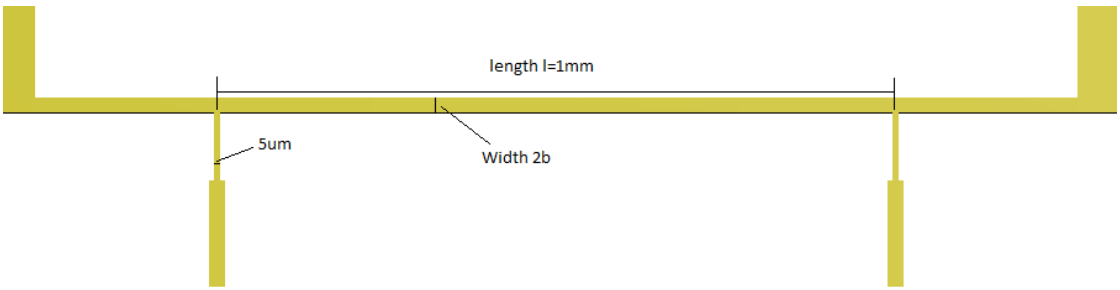

Figure 2.2: Geometry of heater used in 3ω method.

$$\begin{aligned} P(t) &= I(t)^2 R_0 \\ &= I_0^2 R_0 cos(\omega t + \phi_0)^2 \\ &= \frac{1}{2} I_0^2 R_0 + \frac{1}{2} I_0^2 R_0 cos(2\omega t + 2\phi_0) \end{aligned} \tag{2.1}$$

Here R_0 is the resistance of the heater at room temperature. The power $P(t)$ has a DC and a AC component. The AC component has the same magnitude as the DC component but varies with time at 2ω frequency. The average power generated by the heater is:

$$\begin{aligned} \langle P \rangle &= \frac{\omega}{\pi} \int_0^{\frac{\pi}{\omega}} P(t) dt \\ &= \frac{1}{2} I_0^2 R_0 \end{aligned} \tag{2.2}$$

The power generated by Joule heating of the heater dissipates through the thin-film and substrate, causing the temperature of the substrate and the heater to increase above the ambient temperature. The temperature increase depends on the power, frequency of driving current and thermal properties of the sample, particularly thermal conductivity. Since the power has a constant and oscillating components, the temperature rise has both constant and oscillating parts also at 2ω frequency. The temperature rise of the heater can be expressed as [21]:

$$\Delta T(t) = \Delta T_{DC} + \Delta T_{AC} cos\left(2\omega t + 2\phi_0 + \Phi(\omega)\right) \tag{2.3}$$

The heater also acts as a thermometer to detect the temperature change by measuring the resistance of the heater. Within small range of temperature change, the resistance of the heater increase linearly with temperature rise:

$$\begin{aligned} R(T) &= R_0(1+\alpha(T(t)-T_0)) = R_0(1+\alpha\Delta T) \\ &= R_0\left(1+\alpha\Delta T_{DC}+\alpha\Delta T_{AC}cos(2\omega t+2\phi_0+\Phi(\omega))\right) \end{aligned} \tag{2.4}$$

Where α is the temperature coefficient of resistance (TCR), T_0 is the initial temperature of the heater and R_0 is the resistance of the heater at temperature T_0. With resistance at 2ω frequency and current at 1ω frequency, the voltage across the heater is given by:

$$\begin{aligned} V(t) &= I(t)R(t) \\ &= I_0R_0\left\{(1+\alpha\Delta T_{DC})cos(\omega t+\phi_0)+\alpha\Delta T_{AC}cos(2\omega t+2\phi_0+\Phi(\omega))cos(\omega t+\phi_0)\right\} \\ &= I_0R_0\left\{(1+\alpha\Delta T_{DC})cos(\omega t+\phi_0)+\frac{1}{2}\alpha\Delta T_{AC}cos(\omega t+\phi_0+\Phi(\omega))\right. \\ &\qquad\left.+\frac{1}{2}\alpha\Delta T_{AC}cos(3\omega t+3\phi_0+\Phi(\omega))\right\} \end{aligned} \tag{2.5}$$

The voltage across the heater contains both 1ω and 3ω components. The magnitude and phase of the third harmonic $V_{3\omega}(t)$ is related to the thermal properties of the sample and can be measured by a lock-in amplifier. The in-phase and out-of-phase components of oscillating temperature rise can be determined from the measured 3ω voltage by the formula [10]:

$$\Delta T_{AC,x} = \frac{2V_{3\omega,x}}{\alpha I_0R_0} \tag{2.6}$$

$$\Delta T_{AC,y} = \frac{2V_{3\omega,y}}{\alpha I_0R_0} \tag{2.7}$$

The in-phase component of third harmonic $V_3\omega$ is in phase with $3\phi_0$, where ϕ_0 is the phase of driving current; the out-of-phase component is phase shifted by $\Phi(\omega)$ regarding to the in-phase component. The magnitude of 1ω component

of the voltage $V_{1\omega}$ is approximately equal to $I_0 R_0$ when considering the fact that temperature coefficient of resistance is typically much smaller than 1. Then we have:

$$\Delta T_{AC,x} = \frac{2V_{3\omega}}{\alpha V_{1\omega}} cos(\Phi(\omega)) \tag{2.8}$$

$$\Delta T_{AC,y} = \frac{2V_{3\omega}}{\alpha V_{1\omega}} sin(\Phi(\omega)) \tag{2.9}$$

The thermal conductivity of samples is determined by comparing and fitting the measured in-phase and out-of-phase components of ΔT_{AC} with the analytic solution of heat equation.

2.2 Analytic solution of heat equation

The analytic solution of heat equation used in the 3ω method was first proposed by David Cahill [9–11] and varies with different heater geometries. The temperature profile in isotropic substrates is derived for both 1D heater and 2D rectangular. The temperature profile offsets caused by inserting an isotropic thin-film between the heater and the substrate are also carefully discussed.

2.2.1 1D heater solution

Figure 2.3 shows the geometry of the 1D heater discussed here [21]. The 1D heater is a line heater embedded on top of the substrate. We assume the length of the heater is infinite. Thus we can only discuss the thermal transportation in the cross section which is perpendicular to the line heater, and the heater can be treated as a point heat source in such a cross section. We also assume the substrate is isotropic so the thermal conductivity κ and thermal diffusivity D of the substrate is independent of the orientations. We first assume the cross section of the line heater is a semi-circle with radius a, and then take the limit of $a \to 0$ once we get

the temperature profile. Since the thermal conductivity of air is much smaller than

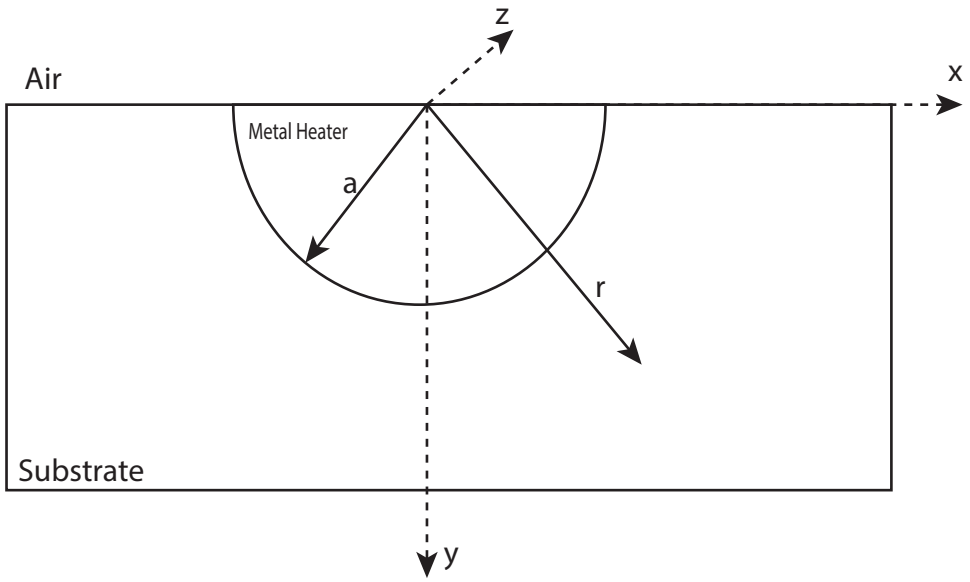

Figure 2.3: Geometry of 1D heater.

the substrate, and the thermal convection between the heater and air is negligible, we assume there is no heat propagates upward. According to the law of heat conduction or Fourier's Law, the heat flux inside the sample can be described as:

$$\vec{Q}(\vec{r},t) = -\kappa \nabla T(\vec{r},t) \tag{2.10}$$

where κ is the thermal conductivity of the material, $\vec{q}(\vec{r},t)$ is the local heat flux density, and $T(\vec{r},t)$ is the temperature profile inside the samples. The thermal diffusivity D is defined as the thermal conductivity divided by the volumetric heat capacity:

$$D = \frac{\kappa}{\rho C_p} \tag{2.11}$$

where ρ is the density and C_p is the specific heat capacity. The thermal diffusivity describes the ability of a substance to conduct thermal energy compared to its ability to store it.

$$\rho C_p \frac{\partial T(\vec{r},t)}{\partial t} = -\nabla \vec{Q}(\vec{r},t) \tag{2.12}$$

Thus the heat equation used to describe the temperature profile of a substance can be expressed as:

$$\begin{aligned} \frac{\partial T(\vec{r},t)}{\partial t} &= \frac{\kappa}{\rho C_p} \nabla^2 T(\vec{r},t) \\ &= D\nabla^2 T(\vec{r},t) \end{aligned} \tag{2.13}$$

Here we define the temperature increase inside the samples as the real part of $\Delta\tilde{T}(\vec{r},t)$, which is a complex function of coordinate $\vec{r}$ and time t [21]:

$$\Delta\tilde{T}(\vec{r},t) = \Delta\tilde{T}_{DC}(\vec{r}) + \Delta\tilde{T}_{AC}(\vec{r}) e^{i(2\omega t + 2\phi_0 + \Phi(\omega))} \tag{2.14}$$

The time-independent DC component of the temperature increase is the steady-state solution of heat equation related to the constant component of power generated by the heater. The oscillating part is caused by the AC component of the power dissipated by the heater. We assume the magnitude of the temperature rise decays to zero at a distance far away from the heater. In the 1D heater geometry, the generated heat flows into the substrate radially, suggesting the temperature rise only depends on the radial coordinate r. Plugging the postulated solution of temperature rise Equation 2.14 into Equation 2.13 gives:

$$\begin{aligned} &\frac{1}{r}\frac{\partial}{\partial r}\left\{ r\frac{\partial \Delta\tilde{T}_{DC}(r)}{\partial r} \right\} + \frac{1}{r}\frac{\partial}{\partial r}\left\{ r\frac{\partial \Delta\tilde{T}_{AC}(r)}{\partial r} \right\} e^{i(2\omega t + 2\phi_0 + \Phi(\omega))} \\ &\qquad = \frac{1}{D}\left\{ \frac{\partial \Delta\tilde{T}_{AC}(r) e^{i(2\omega t + 2\phi_0 + \Phi(\omega))}}{\partial t} + \frac{\partial \Delta\tilde{T}_{DC}(r)}{\partial t} \right\} \\ &\qquad = \frac{1}{D}\left\{ i2\omega \Delta\tilde{T}_{AC}(r) e^{i(2\omega t + 2\phi_0 + \Phi(\omega))} + 0 \right\} \end{aligned} \tag{2.15}$$

The DC and AC components of the temperature rise can be solved separately and the time derivative of the DC component is equal to zero. The steady-state part and the oscillating part of the temperature increase can be solved separately. Equation 2.15 can be separated into:

$$\frac{1}{r}\frac{\partial}{\partial r}\left\{r\frac{\partial \Delta\tilde{T}_{DC}(r)}{\partial r}\right\} = 0 \tag{2.16}$$

$$\frac{1}{r}\frac{\partial}{\partial r}\left\{r\frac{\partial \Delta\tilde{T}_{AC}(r)}{\partial r}\right\} = \frac{i2\omega}{D}\Delta\tilde{T}_{AC}(r) \tag{2.17}$$

The solutions of Equation 2.17 is discussed in details here because the magnitude and phase of the oscillating temperature rise can be used to determine the thermal properties of substrate. Equation 2.17 can be rewritten as:

$$\frac{d^2\Delta\tilde{T}_{AC}(r)}{dr^2} + \frac{1}{r}\frac{\Delta\tilde{T}_{AC}(r)}{dr} - \frac{i2\omega}{D}\Delta\tilde{T}_{AC}(r) = 0 \tag{2.18}$$

We can further rearrange Equation 2.18 as:

$$r^2\frac{d^2\Delta\tilde{T}_{AC}(r)}{dr^2} + r\frac{\Delta\tilde{T}_{AC}(r)}{dr} - r^2\frac{i2\omega}{D}\Delta\tilde{T}_{AC}(r) = 0 \tag{2.19}$$

where

$$q = \sqrt{\frac{i2\omega}{D}} \tag{2.20}$$

Equation 2.19 is easily recognized as zeroth order Bessel's differential equation with a complex argument. The solutions of Equation 2.19 are linear combinations of the zeroth order modified Bessel equation [23]:

$$\Delta\tilde{T}_{AC}(r) = c_1K_0(qr) + c_2I_0(qr) \tag{2.21}$$

Using the boundary conditions of $\Delta\tilde{T}_{AC}(r \to \infty) = 0$, the solutions $I_0(qr)$ can be

ruled out because I_0 diverges as r goes to ∞ [23], thus:

$$\Delta\tilde{T}_{AC}(r) = c_1 K_0(qr) \tag{2.22}$$

According to Fourier's law, the heat flux flows outward at the surface of the heater can be expressed as:

$$\begin{aligned} Q(r=a) &= -\kappa \frac{d\ c_1 K_0(qr)}{dr}\ |_{r=a} \\ &= c_1 \kappa q K_1(qa) \end{aligned} \tag{2.23}$$

Because the total heat flux flows outward at the surface of heater is equal to the average power generated by the heater,

$$\langle P \rangle = \pi l a Q(r=a) = c_1 \kappa q \pi l a K_1(qa) \tag{2.24}$$

where l is the length of the heater. Thus the oscillating temperature rise can be expressed as:

$$\Delta\tilde{T}_{AC}(r) = \frac{\langle P \rangle}{\pi l \kappa q a K_1(qa)} K_0(qr) \tag{2.25}$$

With the limit $a \to 0$, and the fact that $\lim_{a\to 0} qaK_1(qa) = 1$, the oscillating temperature rise with 1D heater is:

$$\Delta\tilde{T}_{AC}(r) = \frac{\langle P \rangle}{\pi l \kappa} K_0(qr) \tag{2.26}$$

Thermal penetration depth is a parameter to determine how deep the thermal waves penetrate into the substrate. In the limit of $|qr| \ll 1$, the first order approximation of $\Delta\tilde{T}_{AC}(r)$ can be expressed as [9, 10, 24] [007]:

$$\Delta\tilde{T}_{AC}(r) = \frac{\langle P \rangle}{\pi l \kappa} \left(\frac{1}{2} ln(\frac{2D}{\omega r^2}) - \gamma - \frac{i\pi}{4} \right) \tag{2.27}$$

where γ is the Euler-Mascheroni constant. From Equation 2.27, the oscillating

temperature rise contains a frequency-dependent real part which is in-phase with the driving current and a frequency-independent imaginary part which is out-of-phase with the driving current. The phase shift of the oscillating temperature rise is defined as:

$$\Phi(\omega) = arctan\left(\frac{Im\Delta\tilde{T}_{AC}(\omega)}{Re\Delta\tilde{T}_{AC}(\omega)}\right) \tag{2.28}$$

and the in-phase (real) and out-of-phase (imaginary) parts can be expressed as:

$$\Delta T_{AC,x}(\omega) = \left|\Delta\tilde{T}_{AC}(\omega)\right| cos\Phi \tag{2.29}$$

$$\Delta T_{AC,y}(\omega) = \left|\Delta\tilde{T}_{AC}(\omega)\right| sin\Phi = -\frac{\langle P\rangle}{4l\kappa} \tag{2.30}$$

When ω is sufficiently small and the thermal penetration depth λ becomes much larger than the half width of the heater [25], the in-phase component of the oscillating temperature $\Delta\tilde{T}_{AC}$ decreases linearly with the driving frequency in logarithmic scale while the out-of-phase component is constant regardless of the frequency of driving current. The derivative of the in-phase component with respect to frequency in logarithmic scale is given as:

$$\frac{d\ \Delta T_{AC,x}(\omega)}{dln(\omega)} = -\frac{\langle P\rangle}{2\pi l\kappa} \tag{2.31}$$

Equation 2.31 provides a way to determine the thermal conductivity of substrate from the inverse slope of such a linear region. If we measure the magnitude of in-phase oscillating temperature rise over a wide range of driving frequencies, then the thermal conductivity of the substrate can be determined by [9]:

$$\kappa = -\frac{\langle P\rangle}{2\pi l}\left(\frac{d\ \Delta T_{AC,x}(\omega)}{dln(\omega)}\right)^{-1} \tag{2.32}$$

According to Equation 2.30, the thermal conductivity of the substrate can also be determined from the out-of-phase component of temperature rise:

$$\kappa = -\frac{\langle P \rangle}{4l\Delta T_{AC,y}} \tag{2.33}$$

2.2.2 2D heater solution

The typically used 2D heater in the 3ω method is a thin strip of metal on top of the samples. The top view of the heater is rectangular and it is assumed that the length of the heater is infinite. Thus we can only discuss solutions of heat equation in a cross section perpendicular to the length of the heater. Figure 2.4 shows the cross-section geometry of the heater. The width of the heater is finite

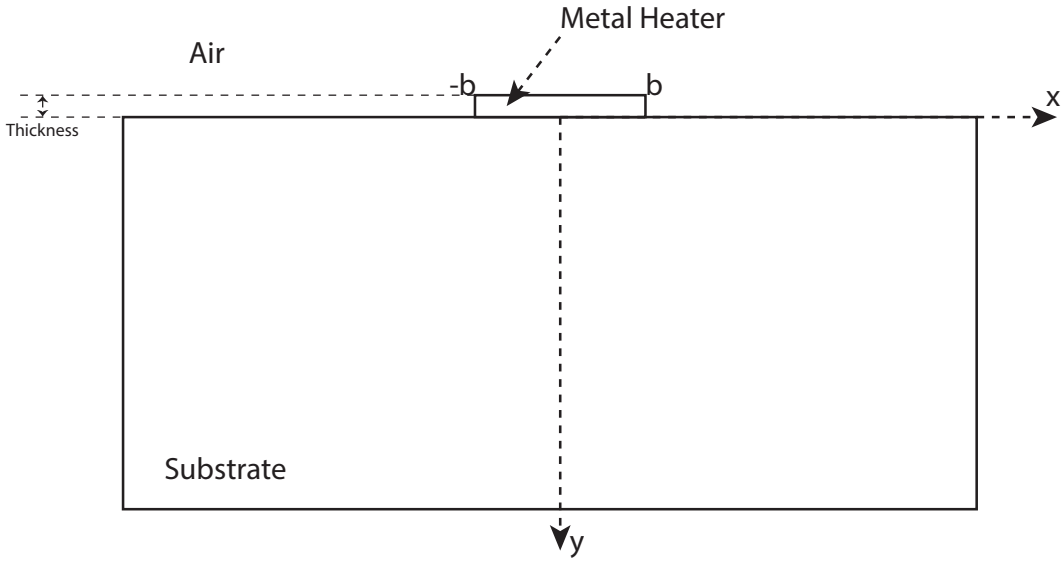

Figure 2.4: geometry of 2D heater on substrate (cross section).

and defined as $2b$ while the height of the heater is typically in the range of hundreds of nanometers. We can get desired heater thickness and desired heater resistance by modifying the deposition parameters of the heater. In the 3ω method, only the temperature rise of the heater is needed to determine the thermal conductivity of the substrate. Thus we only discuss the temperature at the interface of the heater and the substrate (y=0). We further assume the heat flux flowing outward from

the heater is uniform across the interface between the heater and the substrate. Then the 2D heater can be considered as a series of 1D heater on the surface of the substrate. The temperature profile caused by the 2D heater is the convolution of the temperature profile of 1D heater with a rectangular function [21].

$$\Delta\tilde{T}_{AC,2D}(x) = \Delta\tilde{T}_{AC,1D}(x, y = 0) * rect(x) \tag{2.34}$$

where the $*$ represents convolution and the rectangular function $rect(x)$ is defined as

$$rect(x) = \begin{cases} \dfrac{1}{2b} & -b \leq x \leq b \\ 0 & others \end{cases} \tag{2.35}$$

The rectangular function is set to zero for those locations without 1D heaters. The integration of the rectangular function over position is also normalized to one in order to make the total heat flux flowing outward from the 2D heater equal to those of a single 1D heater. Equation 2.26 shows the oscillating temperature increase caused by the 1D heater in cylindrical coordinates. The temperature profile can be rewritten in Cartesian coordinates as a symmetric function about the y-axis, which is $\Delta\tilde{T}_{AC,1D}(x) = \Delta\tilde{T}_{AC,1D}(-x)$. According to the convolution theorem, the Fourier transform of a convolution of two functions is equal to the point-wise product of Fourier transforms:

$$\mathscr{F}\left\{\Delta T_{AC,1D}(x) * rect(x)\right\} = \mathscr{F}\left\{\Delta\tilde{T}_{AC,1D}(x)\right\} \cdot \mathscr{F}\left\{rect(x)\right\} \tag{2.36}$$

The Fourier transform of the rectangular function rect(x) is a sinc function

expressed as:

$$\begin{aligned}\mathscr{F}\left\{rect(x)\right\} &= \int_{-\infty}^{+\infty} rect(x)\ e^{-ikx}dx \\ &= \int_{-b}^{+b} \frac{1}{2b}e^{-ikx}dx \\ &= \frac{sin(kb)}{kb} = sinc(kb)\end{aligned} \tag{2.37}$$

The Fourier transform of $\Delta\tilde{T}_{AC,1D}(x, y = 0)$ is given by [10]:

$$\begin{aligned}\mathscr{F}\left\{\Delta\tilde{T}_{AC,1D}(x, y = 0)\right\} &= 2\int_0^{+\infty} \frac{\langle P\rangle}{\pi l\kappa}K_0(qx)\ dx \\ &= \frac{\langle P\rangle}{\pi l\kappa}\frac{\pi}{\sqrt{k^2+q^2}}\end{aligned} \tag{2.38}$$

Thus the oscillating temperature rise caused by the 2D heater can be determined by the inverse Fourier transform:

$$\begin{aligned}\Delta\tilde{T}_{AC,2D}(x, y = 0) &= \mathscr{F}^{-1}\left\{\mathscr{F}\left\{\Delta\tilde{T}_{AC,1D}(x)\right\}\cdot\mathscr{F}\left\{rect(x)\right\}\right\} \\ &= \frac{1}{2\pi}\int_{-\infty}^{+\infty}\frac{\langle P\rangle}{\pi l\kappa}\frac{\pi sin(kb)}{kb\sqrt{k^2+q^2}}e^{-ikx}\ dk \\ &= \frac{\langle P\rangle}{\pi l\kappa}\int_0^{\infty}\frac{sin(kb)cos(kx)}{kb\sqrt{k^2+q^2}}\ dk\end{aligned} \tag{2.39}$$

Equation 2.39 suggests that the temperature rise caused by the 2D heater is also symmetric about y-axis. As the temperature of the heater increases, the resistance of the heater also increases and is measured in the 3ω method. The resistance of the heater depends on the average temperature of the heater, which can be expressed as [10]:

$$\begin{aligned}\Delta\tilde{T}_{AC,2D}(\omega) &= \frac{1}{2b}\int_{-b}^{b}\frac{\langle P\rangle}{\pi l\kappa}\int_{0}^{\infty}\frac{sin(kb)cos(kx)}{kb\sqrt{k^2+q^2}}\,dkdx \\ &= \frac{\langle P\rangle}{\pi l\kappa}\int_{0}^{\infty}\frac{sin^2(kb)}{(kb)^2\sqrt{k^2+q^2}}\,dk \\ &= \frac{\langle P\rangle}{\pi l\kappa}\int_{0}^{\infty}\frac{sin^2(kb)}{(kb)^2\sqrt{k^2+\frac{i2\omega}{D}}}\,dk \end{aligned} \tag{2.40}$$

The integral in Equation 2.40 can be evaluated numerically. Figure 2.5(a) is a plot of 1D and 2D heater solution numerically calculated by River Wiedle [21]. The in-phase and out-of-phase components of the oscillating temperature rise of the 2D heater are plotted as solid line in Figure 2.5(a) versus the driving frequency on a logarithmic scale. The oscillating temperature rise caused by 1D heater is also approximately evaluated and plotted as dotted line in the same figure. As we can

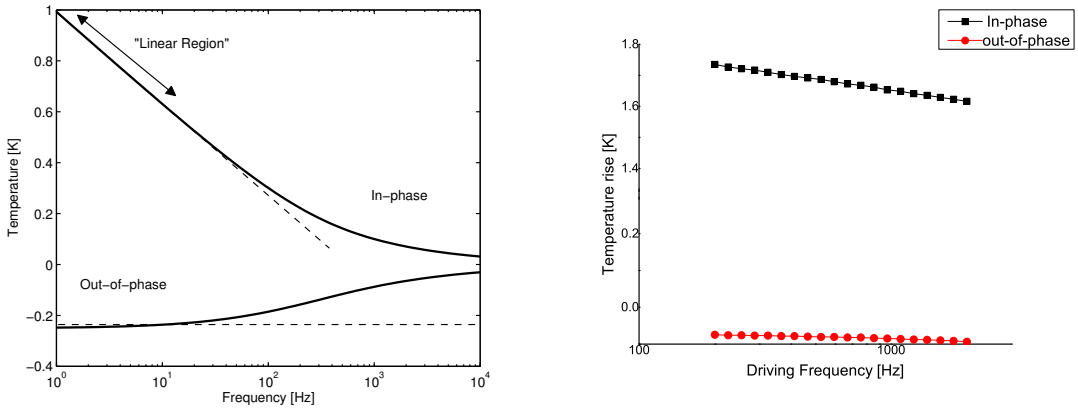

(a) Numerical evaluated ΔT_{AC}

(b) Measured ΔT_{AC}

Figure 2.5: (a) Numerically evaluated temperature rise vs. frequency in log scale for the 2D heater and 1D heater solutions. Here we assume: $\langle P\rangle / l = 1Wm^{-1}, b = 10\mu m, D = 1mm^2s^{-1}$. Figure takes from River Wiedle's thesis; (b) In-phase and out-of-phase temperature rise vs. driving frequency for a amorphous metals sample on p-type silicon substrate.

see, the temperature rise of 2D heater agrees well with that of 1D heater at low frequency. The aluminum heater used in our measurements typically has a length of 1 mm, a width of 5 μm and a thickness of 180 nm. Figure 2.5(b) shows the in-phase and out-of-phase components of temperature rise caused by such heater on top of a amorphous metals sample with p-type silicon substrate. The measured data agrees well with the linear region of the 2D heater model.

The thermal resistance

$$\begin{aligned} \Delta R_{th} &= \frac{\Delta T_{AC}}{Q} \\ &= \frac{2bl}{\langle P \rangle} \Delta T_{AC} \end{aligned} \tag{2.41}$$

where $Q = \frac{\langle P \rangle}{2bl}$ is the heat flux flows outward from the interface between heater and substrate. The units of thermal resistance are $m^2 K M W^{-1}$. The thermal resistance can be further described as [21]

$$R_{th} = \frac{4bl}{\alpha V_{1\omega}^2 I_{1\omega}} V_{3\omega,x} \tag{2.42}$$

According to Equation 2.6 and 2.32, the thermal conductivity of substrate can be determined by the formula [9]

$$\kappa = -\frac{\alpha V_{1\omega}^2 I_{1\omega}}{4\pi l} \left(\frac{dV_{3\omega,x}(\omega)}{dIn(\omega)}\right)^{-1} \tag{2.43}$$

2.2.3 Thin film approximation

When a thin film with thickness of d_f is inserted between the 2D heater and the substrate as depicted in Figure 2.6, and with the assumption that the film thickness d_f is much smaller than the width of the heater $2b$ ($d_f \ll 2b$), the heat flux through the thin film is mainly cross-planar while the in-plane heat flow inside the films is negligible. Under such assumption, the heater can be consider as infinitely wide.

Thus the edge effects of the heater can be ignored and the heat flow should be perpendicular to the interface between the heater and the thin film. Figure 2.7 shows the heat flux pattern inside the thin film when the heater width is much greater than film thickness $2b \gg d_f$ as well as when the heater width is much smaller than film thickness $2b \ll d_f$. As we can see here, for narrow heater, the heat flux is radial within thin film and the narrow heater can be described as a 1D heater; for wide heater, the heat flow pattern inside thin film is cross-planar

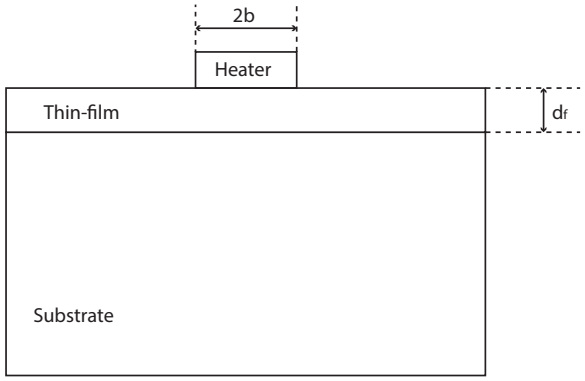

Figure 2.6: Cross-section schematic of thin film on substrate.

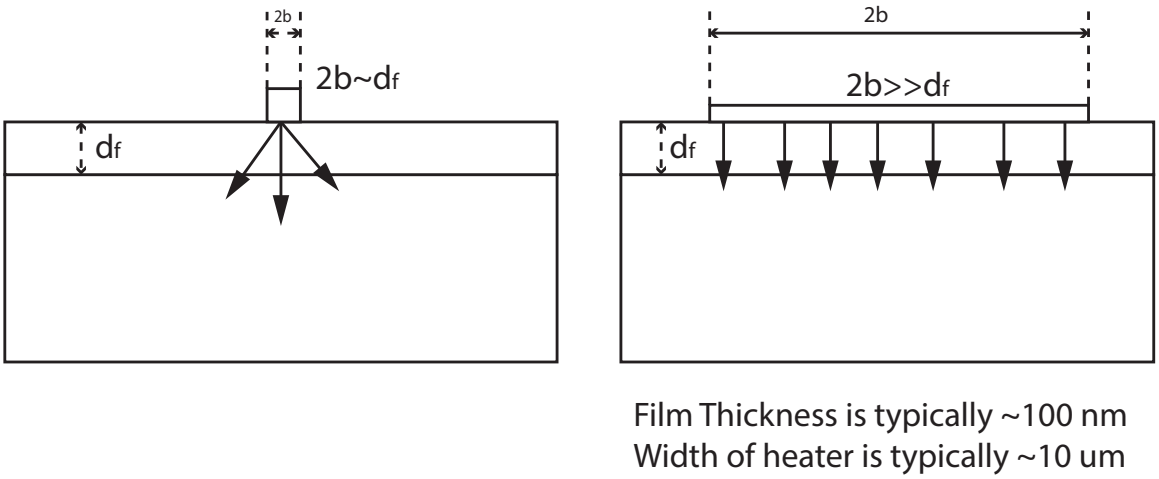

Figure 2.7: Pattern of heat flux inside thin film for $2b \ll d_f$ and $2b \sim f_f$

but gradually switches to radial far away from the heater [21]. At low driving frequency region where the thermal penetration depth is much larger than the film thickness, the behavior of temperature rise of film/substrate system is similar to the substrate-only system. The thickness of films is typically hundreds of nanometers. Thus we can assume the thermal mass of the film is small and the temperature rise of thin films can respond instantaneously to the oscillating driving current. The temperature at the interface between film and substrate should be the same as the temperature at the surface of the 2D heater for substrate only system. We can treat the thin film as a thermal resistance and calculate the temperature rise at the interface between heater and films by applying Fourier's law [26]:

$$Q_y = -\kappa_f \frac{d\Delta T_f}{dy} \tag{2.44}$$

where Q_y is the heat flux through the film as well as the heat flux flows outward from the heater, κ_f is the thermal conductivity of the film and ΔT_f is the oscillating temperature rise with the films. The heat flux is assumed to be constant across the surface of the heater. Thus $Q_y = \frac{\langle P \rangle}{2bl}$. And additional temperature rise caused by the film can be expressed as:

$$\Delta T_f = \int_0^{d_f} \frac{\langle P \rangle}{2bl\kappa_f}\, dy = \frac{\langle P \rangle\, d_f}{2bl\kappa_f} \tag{2.45}$$

According to Equation 2.45, in the low frequency region where the thermal penetration depth is much larger than the film thickness ($\left|\frac{1}{q}\right| \gg d_f$), the film inserted between the heater and the substrate causes a frequency-independent additional offset to the in-phase component of the temperature rise of the heater. Because the thermal mass of the film is negligible and the heating of the film is instantaneous, there is no phase-shift caused by the film. Thus the the out-of-phase component remains unchanged. According to Equation 2.41, the temperature rise can be converted to thermal resistance. The additional thermal resistance caused by the films can be expressed as [26]:

$$\Delta R_{th,f} = \frac{\Delta T_f}{Q_f} = \frac{d_f}{\kappa_f} \tag{2.46}$$

From Equation 2.46, thicker films cause larger thermal resistance and films with smaller thermal conductivity also cause larger additional thermal resistance. We can do the 3ω measurements for a set of film/substrate samples which are identical except for the film thickness and then plot the thermal resistance offset versus the film thickness. The thermal conductivity of the films can be determined from the inverse slope of such plot [26]:

$$\kappa_f = \left(\frac{d \;\; \Delta R_{th,f}}{d \;\; d_f} \right)^{-1} \tag{2.47}$$

2.3 Numerical analysis of the 3ω method based on finite element method

In the previous section, the heat equation was solved for ideal 1D and 2D heaters on thick substrate as well as with the thin film approximation. These analytic solutions require several assumptions: the substrate is semi-infinite, the length of the heater is infinite, film thickness is much smaller than the width of the heater ($2b \ll d_f$), the heater has a negligible thickness, and there is no heat exchange with air during the measurements, the ideal 2D heater has a uniform and negligible thickness as well as uniform width and length. The realistic heaters fabricated by photolithography and lift-off process have inevitable non-uniformity at the edges. Moreover, the heaters produced from wet etch process can be in shape of a trapezoid because of the possible side etching during the process. In order to determine the effects of these assumptions, we have developed an numerical simulation approach in which the time-dependent heat transfer problems of substrate/film/heater system with arbitrary geometry is solved based the finite element method using COMSOL multiphysics software [27–29]. The finite element method is a numerical approach to find the approximate solutions to boundary value problems for differential equations. The equation solved in time-dependent

heat transfer model of COMSOL is:

$$\rho C_p \frac{\partial T}{\partial t} + \rho C_p \vec{u} \cdot \nabla T = \nabla \cdot (\kappa \nabla T) + Q \tag{2.48}$$

where ρ is the density, C_p is the specific heat capacity in units of $J/(Kg{\cdot}\mathrm{K})$, κ is the thermal conductivity, Q is heat sources other than viscous heating and $\vec{u}$ is the velocity vector of the fluid which is zero in our case. The oscillating temperature field at different times can be obtained from the numerical simulation approach. The magnitude and phase of the temperature oscillation at the interface between the heater and substrate is of particular interest. The general geometry of a sample for the 3ω method should be solved using three-dimensional (3D) mesh. A 3D mesh is also needed to study the effects of finite heater length on the analytic solutions. When applying current, the current density is nonuniform inside the heater, thus the heat power generated is also nonuniform. The effects of nonuniform distribution of heat power can be simulated by coupling the electric currents(ec) module, the joule heating (jh) module and the heat transfer in solids (ht) module and need to be solved using 3D mesh. But here we only present basic simulation work to demonstrate the capability and principles of the numerical simulation approach. When the length of the heater is much longer than the thermal penetration depth, heat flux will be mainly inside the cross section that is perpendicular to the length of the heater. The simulation can be simplified to two-dimensional.

First, we simulated the frequency response of temperature oscillation at the interface between heater of 10 μm width and silicon substrate. As in figure 2.8, the structure consists of a metal strip with width 10 μm deposited on top of a silicon substrate.

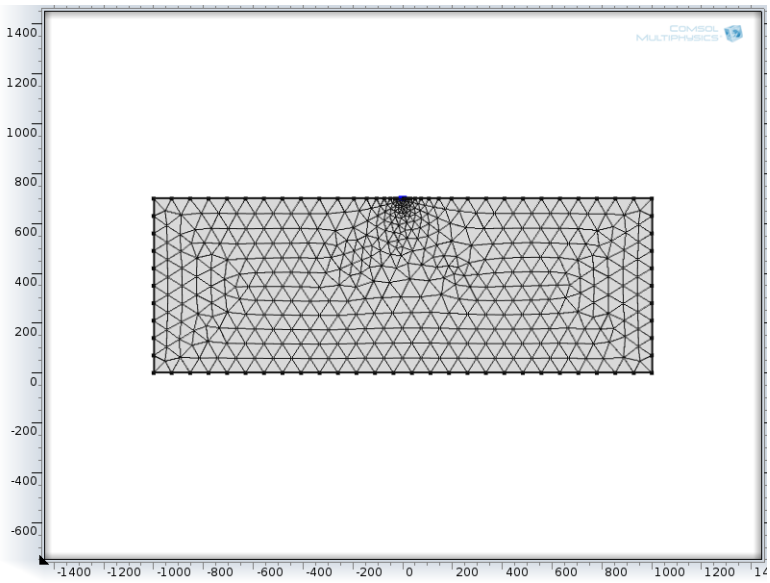

Figure 2.8: Geometry of simulated structure which contains a $10\mu m$ heater on top of silicon substrate. (Units: μm)

The physical properties of materials used for the simulations are found from literature and listed in Table 2.1. The heat flux at the interface between the heater and the substrate is assumed to be uniform and is set to be $5\times10^6 W/m^2 \cdot cos(2\omega t)$. The temperature at the side faces and bottom of the structure is fixed to room temperature ($T = 300K$) and upper surface (except the heater) is set to have a heat exchange with air by convection with the coefficient of thermal convection as $H = 3W \cdot m^{2\cdot}{}^{\circ}\mathrm{C}$.

Figure 2.9 shows the temperature oscillation at the center of the heater-substrate interface for silicon substrate. The heat flux at the interface is oscillating at frequency of 2000 Hz. The period of the oscillating temperature can be easily determine from the plot as 5e-4 s. Thus the frequency of the oscillating temperature is 2000 Hz which is consistent with the frequency of the heat power. The magnitude and phase of the temperature oscillation is can also determined from the plot. The magnitude of the oscillating temperature is half of the difference between the maximum and minimum of the plot. Figure 2.9 also suggests that the respond

oscillating temperature has a phase shift compared to the heat power $cos(2\omega t)$. The phase shift in figure 2.9 is $\frac{0.00027-0.00025}{0.00025} \times 90° = 7.2°$. Simulations need to be performed for several different frequencies in order to get the frequency response of such oscillating temperature. Figure 2.10 shows the temperature oscillation of

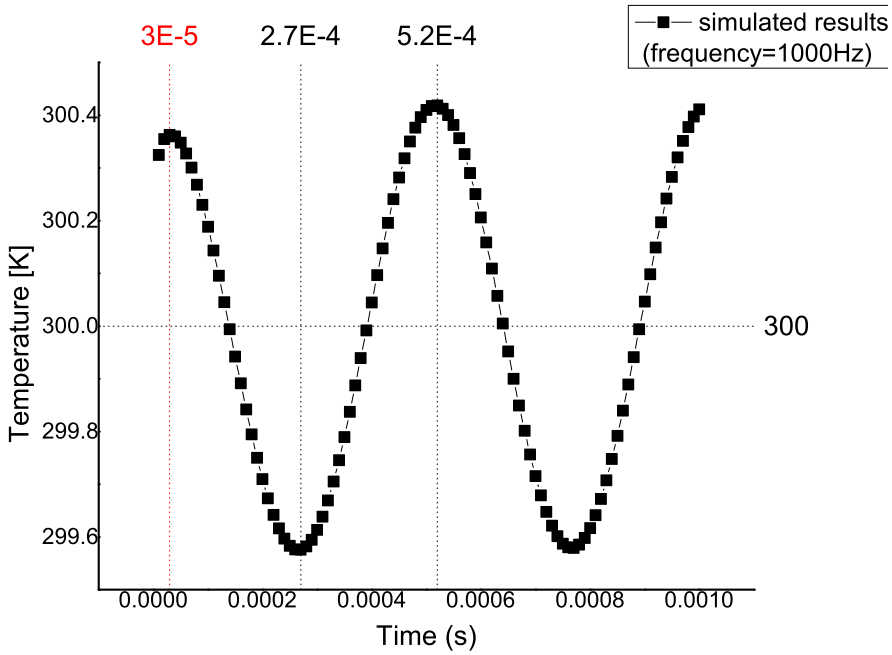

Figure 2.9: Simulated oscillating temperature at the center of the heater-substrate interface for silicon substrate with driving current at 1000Hz.

the center of the heater-substrate interface for silicon substrate at different driving frequencies (10000Hz, 1000Hz, 100Hz, 10Hz, 1Hz from left to right). For each frequency, the time-dependent temperature is simulated for a period. The oscillating temperature is then plotted together using log scale X axis. As we can see in figure 2.10, the magnitude of the oscillating temperature is increased as the frequency is decreased and it turns to flat when the frequency is extremely low (10Hz and 1Hz). According to Equation 2.20, the thermal penetration depth becomes comparable to the size of the substrate at sufficiently low frequency. From

figure 2.10, we also know that the phase of the oscillating temperature is increased as the frequency is increased.

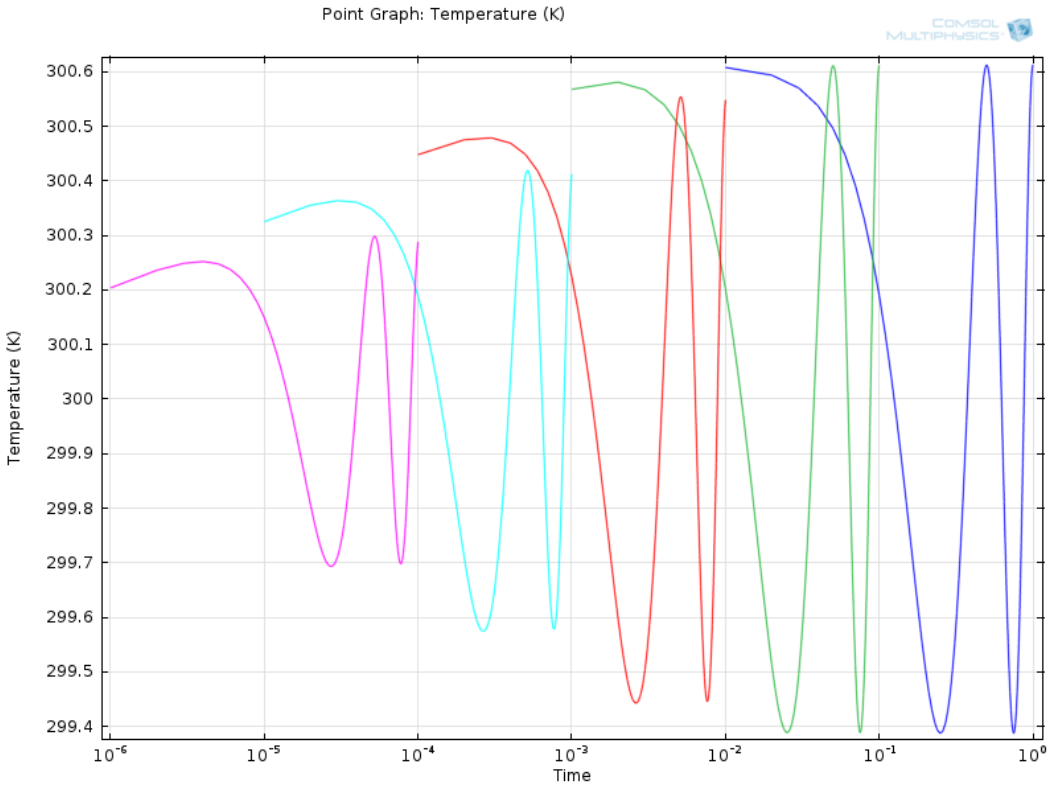

Figure 2.10: Simulated oscillating temperature of the center of the heater-substrate interface for silicon substrate at different driving frequency. X axis is in log scale.

This numerical approach can be extended to simulate the oscillating temperature field of the heater/films/substrate system. And the simulation results can be used to determine the temperature oscillation of the heater even if the film thickness is comparable or larger than the width of the heater. Similar simulations were tried for a 10 μm heater over different thickness of hafnium oxide films on top of silicon substrate. The simulated structure is showed in figure 2.11. In order to reduce the time consuming in running the simulation, the size of the substrate was chosen as 150 μm in length and 100 μm in height, which is much smaller than

the actual size of sample used in the 3ω measurement.

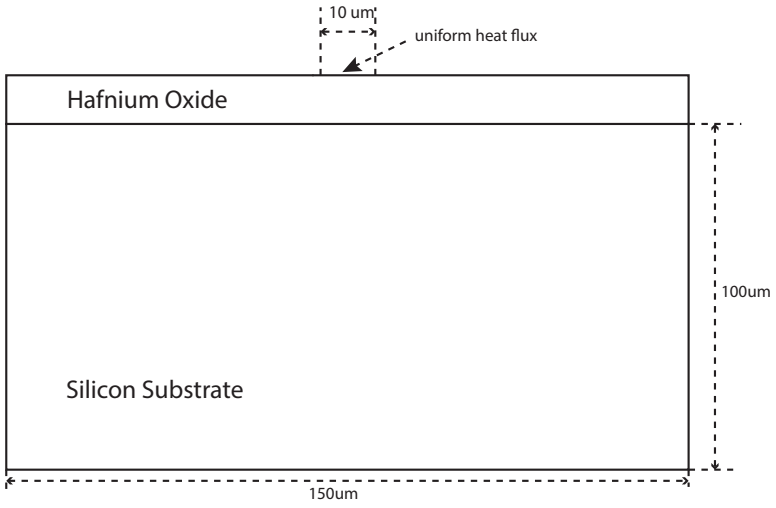

Figure 2.11: Geometry of simulated structure which contains a $10\mu m$ heater on top of a hafnium oxide sample. (not to scale)

For each frequency and each film thickness, the magnitude and phase of heater temperature oscillation need to be calculated from the temperature oscillation plot. It is difficult to interpret such simulated results. The simulation using a small geometry (figure 2.11) is not sufficient for getting reasonable results. For further work on such numerical approach of the 3ω method, the size of the simulated substrate need to be carefully determined respect to the driving frequency and thermal properties of substrate. The mesh inside thin films also need to be refined and optimized in order to get converging and reliable solutions.

Table 2.1: Properties of materials used for the simulations[a].

Material	Density $[kgm^{-3}]$	Specific heat $[Jkg^{-1}K^{-1}]$	Thermal conductivity $[Wm^{-1}K^{-1}]$
Silicon	2330	711	148
HfO_2	9680	120	0.78[b]

[a] Data obtained from literature [14, 30–32]

[b] Thermal conductivity of hafnium oxide is measured.

2.4 Thermal transportation mechanism of amorphous metals

This section is a brief literature review of the thermal conduction mechanism of amorphous metals [33–36]. Electron and phonon are both heat carriers in metals. Thus heat conduction in metals is due to the combined contribution of electrons and phonon:

$$\kappa = \kappa_e + \kappa_p \tag{2.49}$$

For crystalline metals, the electron contribution is dominated the phonon contribution because electrons nearly free inside crystalline metals. Amorphous metals have a homogeneous structures without long range of order. Electrons inside amorphous metals typically show a extremely short elastic mean free path, and as a consequence, the electrical resistivity of amorphous metals is increased and the electron contribution to heat conduction is reduced below the contribution of phonon [33]. Together with the fact that structures of amorphous materials less efficient in conducting heat compared to the crystalline structured materials, the thermal conductivity of amorphous materials is typically lower than the thermal conductivity of crystalline materials [22,37]. The electron contribution to the heat conduction can be described by Wiedemann-Franz law based on the fact that the electronic contribution to heat conduction and electrical transport both involve the nearly free electrons inside the metal. The Wiedemann-Franz law can be expressed as [38]:

$$\kappa_e = \frac{L}{\rho_0} T \tag{2.50}$$

where L is a constant $2.45 \times 10^{-8} W\Omega K^{-2}$, often named Lorenz number, T is the temperature and ρ_0 is the electrical resistivity. The Wiedemann-Franz law is a empirical law with limitations and the value of L has been showed to be not exactly the same for all the materials [39][013]. The Lorentz number has also been showed to have a strong dependency on certain system parameters and the value of L can be reduced in certain cases [40,41]. According to Equation 2.50, the heat conduction contributed by electrons decreases as the electrical resistivity increases and increases as the temperature increases. On the other hand, the phonon thermal

conductivity can be further expressed as [33]:

$$\kappa_p = (\frac{1}{\kappa_p^e} + \frac{1}{\kappa_p^d})^{-1} \tag{2.51}$$

where κ_p^e and κ_p^d indicate the lattice thermal conductivity limited by electron and disorder scattering respectively. A reliable model that can give the phonon thermal conductivity of amorphous metals over a wide temperature range is still lacking. But there are limited models that can sufficiently describing the phonon thermal conductivity of certain amorphous insulators over a small range of temperature. For instance, the standard tunneling model can be used to explain the $T^{1.8}$ dependence of thermal conductivity of amorphous solids below $1K$ [42]. In this theory, the phonon scattering at low temperatures is dominated by the resonant interaction between phonon and the two level systems (TLS) [43,44]. The phonon thermal conductivity of amorphous metals has been observed to be relatively constant over the temperature range of interest [33, 34].

The properties or characteristics, such as thermal conductivity, resistivity and temperature coefficient of resistance, of thin film materials is typically different from those of the corresponding bulk materials, especially when the film thickness is below the bulk mean free path for electrons or phonon [45]. Tab 2.1 of [22] shows the thermal conductivity of several materials both for thin-film and bulk, suggesting that the thermal conductivity of thin films materials is typically smaller than that of bulk materials.

The expected value for thermal conductivity of amorphous metals, thermal conductivity of several other amorphous metals from literature as well as of elements in our materials listed in Table 2.2.

Table 2.2: Summary: Thermal conductivity of several amorphous metals and constituted elements of TaWSi from literature.

Material	Thermal conductivity $[Wm^{-1}K^{-1}]$	Comments
Tantalum	57	bulk [46]
Tungsten	174	bulk [46]
Si	150	bulk [46]
$Tb_{21}Fe_{73}Co_6$	4.5	[34]
$Gd_{21}Fe_{72}Co_7$	5.5	[34]
$Fe_{80}B_{20}$	10.0	[34]
$Fe_{32}Ni_{36}Cr_{14}P_{12}B_6$	6.6	[34]
$Zr_{47}Cu_{31}Al_{13}Ni_9$	4.5 (amorphous) 5.0 (crystalline)	TDTR [18]
$Zr_{56.2}Ti_{13.8}Nb_{5.0}Cu_{6.9}Ni_{5.6}Be_{12.5}(at\%)$	5.29	Liquidmetal Technologies [2]
$Zr_{55}Cu_{30}Al_{10}Ni_5$	5.02	bulk [47]
$Zr_{41}Ti_{14}Cu_{12}Ni_{10}Be_{23}$	4.59	bulk [47]
$Pd_{40}Ni_{40}P_{20}$	7.03	bulk [47]
$Pd_{40}Ni_{20}Cu_{20}P_{20}$	6.25	bulk [47]
$Pd_{40}Ni_{10}Cu_{30}P_{20}$	5.11	bulk [47]

The minimum thermal conductivity model has been successfully used to describe the thermal conductivity of amorphous dielectrics around $100K$ [35]. This model was originally proposed by Einstein and further improved [34, 35]. Einstein treated the atomic vibrations of a solid as coupled harmonic oscillators with same vibrating frequency. The thermal conductivity is due to the random walk between these localized harmonic oscillators and can be expressed as [35]:

$$\kappa_{min} = (\frac{\pi}{6})^{1/3} k_B n^{2/3} \sum_i v_i (\frac{T}{\Theta_i})^2 \int_0^{\Theta_i/T} \frac{x^3 e^x}{(e^x - 1)^2} dx \tag{2.52}$$

where k_B is the Boltzmann constant, v_i is the speed of sound inside the material and $\Theta_i = v_i(\hbar/k_B)(6\pi^2 n)^{1/3}$ with n as the number density of atoms. To calculate the minimum thermal conductivity, the speed of sound for two transverse and one longitudinal modes inside the solid need to estimated or simulated. This model does not fully describe the thermal conductivity in amorphous metals because it does not address the electron contribution and the strong electron-phonon coupling effect. But it is possible to use the minimum thermal conductivity model to roughly estimate the thermal conductivity of amorphous metals before the actual measurements.

Chapter 3: Instrumentation, Materials and Methods

This chapter first describes the preparation of samples for determining their room temperature thermal conductivity via the 3ω method. The material of interest are prepared as thin films by the combination of several deposition process. A thin strip of metal is then deposited on the surface of the sample and functions as both heater and thermometer. The size and uniformity of the heater are critical to obtain reliable measurements and to determine the thermal conductivity. The features of the heaters are patterned by photolithography and a lift-off process.

This chapter then discuss the circuits and set-up for measuring the 3ω voltage across the heater. The temperature coefficient of resistance (TCR) is a important parameter in converting the measured 3ω voltage to thermal resistance and determining the thermal conductivity. Thus the method used to determine TCR of heaters is also described here in details.

3.1 Sample preparation

The thermal conductivities of hafnium oxide, silicon nitride and amorphous multi-component metals TaWSi have been determined via the 3ω method. The detailed procedures of preparing those samples are discussed in this section. Samples of HfOx, SiNx and TaWSi are prepared in the clean room at HP campus and the Owen cleanroom at OSU campus. Typically a set of four samples, identical at all aspects except the film thickness of the material, are needed to determine the thermal conductivity of the material. For the amorphous metal samples, an additional insulation layer is needed between the metal heater and the amorphous metal thin films.

3.1.1 Growth

The typical size of samples is $1'' \times 1''$. The substrate of samples is p-type silicon with $\langle 100 \rangle$ orientation with resistivity 5-35 $ohm \cdot cm$. A 100 nm thick layer of thermally grown silicon dioxide is on top of the silicon substrate. The thickness of the thermal oxide is 100 nm for all the samples. Thus the thermal resistance offset caused by the thermal oxide layer can be canceled out when we isolates the contribution of the thin film materials of interest. All the thin films of HfOx, SiNx and TaWSi are deposited on top of the same p-Si/SiO_2 substrates.

The amorphous multicomponent metals TaWSi are deposited by DC magnetron sputtering in the cleanroom at HP campus. The DC magnetron sputtering can deposit materials even with high melting points and the sputtered films typically have a composition close to the target and good adhesion to the substrate. A set of four TaWSi samples of thickness 200 nm, 250 nm, 300 nm and 400 nm is needed to determine the thermal conductivity of TaWSi. An additional electrically insulate and thermally conduct layer of hafnium oxide is needed between the metal heater and the amorphous metal films. The hafnium oxide films are deposited on top of the amorphous metal films by atomic layer deposition (ALD) in the cleanroom at HP campus. The thickness of hafnium oxide is the same for each set of TaWSi samples. ALD has very accurate control of the film thickness but is very slow. With the concerns of possible electrically breakthrough for thin hafnium oxide films, four sets of TaWSi samples are produced and the thickness of hafnium oxide varies among different sets of samples. The thickness of hafnium oxide films are 24.4 nm, 40 nm, 60 nm and 80 nm. The threshold thickness and the suitable thickness of hafnium oxide films are experimentally determined based on the measurements on these four sets of TaWSi samples. Figures 3.1 shows the geometry of the amorphous metals sample.

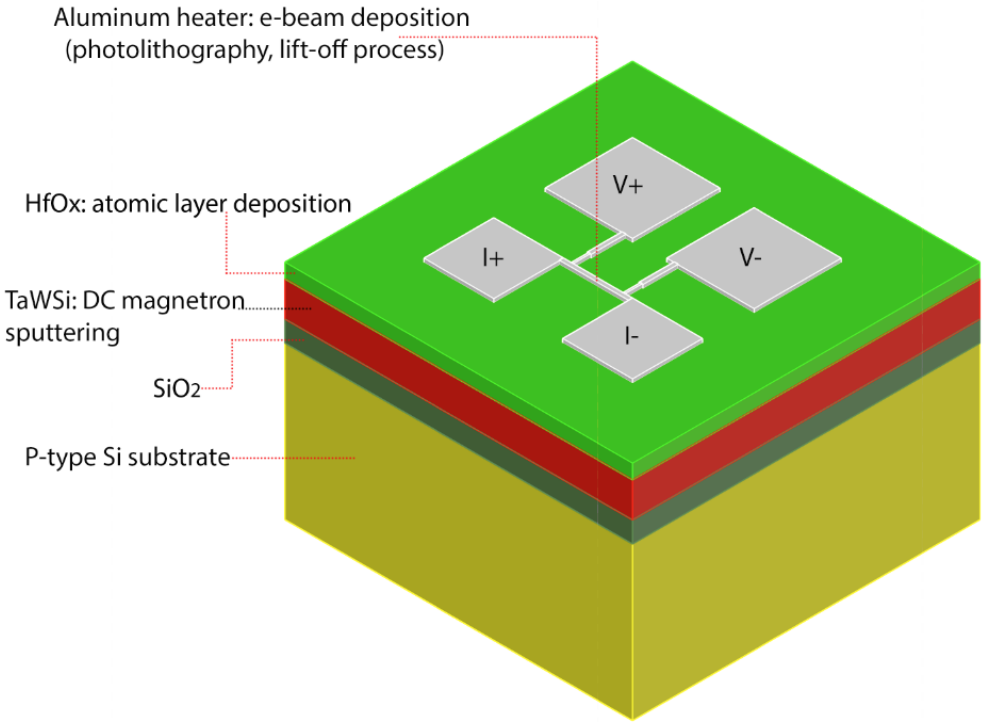

Figure 3.1: Substrate geometry of amorphous metals sample used in the 3ω method.

Moreover, a set of hafnium oxide samples with different film thickness 24.4 nm, 40 nm, 80 nm are produced by atomic layer deposition at HP campus and are used to determine the thermal conductivity of hafnium oxide as well as to provide reference for the amorphous metal measurements. The silicon nitride samples with different film thickness of 100 nm, 200 nm, 300 nm, 400 nm are produced in the cleanroom at HP campus and are used to determine the thermal conductivity of silicon nitride.

3.1.2 Heater masks

Efforts have been made previously to produce the heater by shadow-masking deposition but the resulting features of the heater ends up not well enough for the

3ω measurements. The heaters used in the measurements are patterned by photolithography using the mask aligner in Owen cleanroom at OSU campus. The mask for the photolithography is produced by direct write laser lithography using the DWL 66 tool in Owen cleanroom, with the help of Fanghui Ren from Alan Wang's group. The heater pattern is created using AutoCAD following the design rules of DWL 66. Figure 3.2 shows the geometry of the heater typically used in the 3ω measurements. A long strip of metal is the heater as well as the thermometer. Two contact pads at the end of the metal strip are used to apply a current to the heater. Other two contact pads at the side of the heater are connected to the heater via two strip of metal path and are used to measure the 3ω voltage as well as the 1ω voltage across the heater. The idea of using four contact pads is similar to the idea of 4-point probe used in resistivity measurements. The voltage probe does not affect the current through the heater. The width of the metal path that connect the voltage pads to the heater reduce to $5\mu m$ in order to minimize the voltage inaccuracy caused by the finite size of metal path. In order to apply the 2D heater solution discussed in chapter 2, the geometry of the heater must be exactly rectangular and the length of the heater should be much larger than the width of the heater. Any roughness at the side edge of the heater will cause inconsistency of the heater width and limits the accuracy of the measurements. The length of the heater is 1 mm while the width are 10 μm, 15 μm and 20 μm for different heaters. Typically several heaters with different width can be patterned on top of the samples, which can increase the possibilities of getting high quality heaters as well as can determine the effects of heater width and anomalies on the accuracy of the measurements.

The DWL 66 pattern generator is essentially a photoresist exposure system. To make a photolithography mask, the starting mask blanks are essentially a $4'' \times 4''$ piece of glass, coated with a thin layer of chrome and topped with a very uniform layer of photoresist. Mask blanks are then loaded into the system. The 10 mm laser write head which can define features down to about 2.5 μm is used to expose

selected areas to ultraviolet light based on the design file in the computer controller. After the pattern, the mask is placed into a dish of developer to remove the photoresist that was exposed to the ultraviolet light. Then the mask is placed into a dish of chrome etchant to remove only the chrome that is no longer protected by photoresist. The mask is finally complete after removing the remaining photoresist. Due to the possible side etching when placing the mask into the chrome etchant, the actual width of heaters on the mask is slightly greater than the designed values. Thus the width of heaters must be measured individually under the microscopy after the whole process. Two patterns are generated on different areas of the same mask. One is written directly based on the design file while the other one is written based on the inverting of the same design file. Thus with the same negative photoresist, the heaters can be patterned by both lift-off and etching with the use of different areas of the mask.

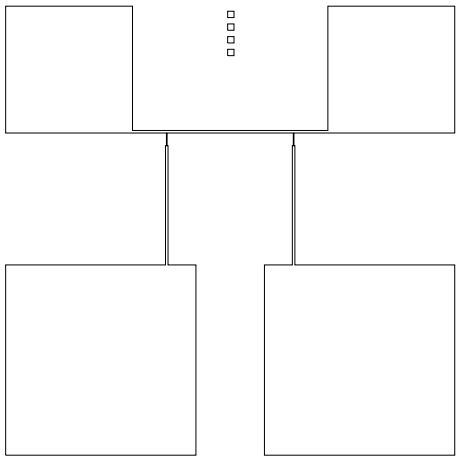

Figure 3.2: Geometry of heater used in the 3ω method

3.1.3 Photolithography and possible procedure to improve the heater quality

Photolithography and lift-off process have proven capable of producing usable heaters for the 3ω measurements. Two major requirements regrading the quality of the heater features are: uniform width and edges of the heater and good adhesion between the deposited heater and the surface of the samples. The photolithography process is sensitive to environment parameters, such as temperature and humidity. They are difficult to control so it is difficult to get identical photolithography patterns. A recipe for photolithography is presented here, but modifications are expected. A useful and practical idea is to start the whole photolithography process using a spare sample every time and modify the recipe accordingly.

1. The samples are first cleaned by rinsing with acetone, isopropyl alcohol (IPA) and 18 $M\Omega \cdot cm$ deionized water in order. Samples are blown dry with nitrogen airbrush and baked on a 115 °C hot plate for 2 minutes to further remove the remaining water. The sample cleaning is performed by acetone which is a good organic solvent and easily evaporate. IPA is used to remove the acetone together with dirt dissolved in acetone. DI water is then used to remove IPA. The cleaning procedure described here is sufficient for the samples which are produced in a higher-class cleanroom at HP campus. A better job of sample cleaning can improve the edges uniformity in the patterning and adhesion in the heater deposition. To perform a more thorough cleaning, the samples can be put in acetone, IPA and DI water in order and each for a 15 minutes ultrasonic bath.

2. Sufficient drops of MicroChem MCC 80/20 photoresist primer are put on the sample to cover the whole surface. After 30 seconds to allow the primer spread out the sample is spun at 3000 RPM for 10 seconds and then at 4000 RPM for 20 seconds to achieve a uniform distribution of photoresist primer. The 80/20 photoresist primer can increase adhesion of photoresist to the sample surfaces and can pre-wet the samples so the photoresist spreads more easily. It can also improve the wet etch performance. Following this the sample is baked on a 115 °C hot plate for 2 minutes.

3. Sufficient drops of S1818 photoresist are put onto the sample to cover 2/3 of the surface. Immediately the sample is spun at 3000 RPM for 10 seconds and then at 4000 RPM for 20 seconds to achieve a uniform distribution of photoresist. Air bubbles in the photoresist should be avoided because they cause nonuniform distribution of photoresist. The thickness and uniformity of resulting photoresist layer depends on the spinning velocity, spinning time, total amounts of photoresist, the existence of air bubbles or dirt on samples, the length of waiting time between application of the photoresist and starting the spinning and so on. Typically, the resulting thickness of photoresist is about 1-2 μm and is good enough for heater patterning. Following this the sample is soft-baked on a 85 °C hot plate for 2 minutes.

4. The chrome mask and the sample are aligned and brought into contact using the SUSS MJB3 mask aligner. Then the spin-coated photoresist is exposed to ultraviolet light through the mask for 22.5 seconds. The lamp power has been calibrated to 275 Watt. The long exposure time is because the lamp is failing and is approaching to the end of its lifetime. The power distribution across the exposure window is also very nonuniform. Each sample ($1'' \times 1''$ size) has been placed as close to the center of the exposure window as possible. Only heaters at the center of the sample a good quality while the rest poor quality. The failing UV lamp is the major obstacle to producing usable heaters.

5. The photoresist is then developed in a solution which contains 5:1 (volume ratio) DI water to Microposit 351 developer. The photoresist exposed to ultraviolet light becomes soluble and dissolves in the solution while the unexposed photoresist remains untouched. The developing time used here is about 1 minute. The slightly longer developing time is because the failing UV lamp has caused under-exposure of the photoresist and longer time is needed to dissolve such under-exposed photoresist. The ambient temperature also affects the developing time. By putting the dish of developer on hot plate, the developer can be heated up to a temperature slightly higher than the room temperature and is less likely be affected by the fluctuating room temperature.

6. After the developing, the sample is cleaned with DI water and blown dry with a nitrogen airbrush. Then an aluminum film is deposited on top of the samples by e-beam deposition. Follow this is a lift-off process to remove the aluminum which sits on top of photoresist.

Figure 3.3 shows an example of bad featured heater. The bright area of the heater is much larger than the designed size and is clearly underexposed, suggesting that the photoresist is exposed to diffracted UV light. Thus the mask and the sample are actually not in contact during UV exposure. More specifically: The sample is held to the stage by vacuum to increase stability of samples during the exposure. The size of our sample is smaller than the stage so several other spare substrates have been used to cover the open vacuum holes. The extra spare substrates are imperceptibly thicker than the sample so the mask is not in contact with the sample. So the spare substrates used to cover vacuum holes of the stage need to be thinner than the sample. The mask can get photoresist residue or

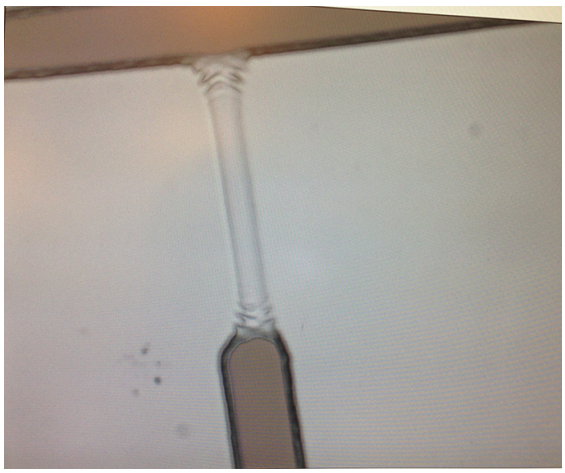

Figure 3.3: An example of bad heater

other dirt when brought into contact with the sample during exposure. The mask must be cleaned with acetone, IPA and DI water after every use to maintain the usability.

The adhesion of the heater to the sample is critical for the thin film measure-

ments. Several procedures can be taken to improve the adhesion of the heater: soft-bake for 2 minutes after developing to further dry out the samples; hydrogen plasma cleaning of the samples after developing; instead of a lift-off process, first depositing the aluminum films and then perform an aluminum etching after the photolithography.

3.1.4 Heater deposition

The heater also acts as a thermometer by measuring the temperature-dependent resistance of the heater. The typical temperature rise of the heater during the 3ω measurements is about or even smaller than 1 K. Metals with high resistivity and large temperature coefficient of resistance (TCR) are preferable for the heater material to maximize the magnitude of the 3ω voltage signal. The resistivity and TCR of deposited metal films depend especially on the deposition process and can be significantly different from the bulk value for metals that can easily oxidize during deposition. Nevertheless, the resistivity and TCR of bulk metals can be used as reference to find the suitable material for the heater. The adhesion of heater to the substrate is extremely important for thin film measurements because a good adhesion will reduce the mismatch of phonon velocity at the interface and as a result reduce the interface thermal resistance. Aluminum and nickel are both good candidate for the material of the heater. Aluminum has been chosen because it has been proved to be a reliable heater material in previous measurements. The heaters are deposited by electron beam evaporation performed by Greg Angelos from John Wager's group. With the width of the heater as 10 μm, 15 μm or 20 μm and the length of the heater as 1 mm, the thickness of the aluminum is chosen as 180 nm to make the heater resistance reasonably large. E-beam deposition has several advantages compared to thermal deposition: the particle of the e-beam deposition has a higher kinetic energy and can achieve a better adhesion of the aluminum film to the sample; heaters deposited by e-beam is more uniform at the edges because the lack of shadowing in the thermal deposition; e-beam tool has a better vacuum and can decreases the possibilities of aluminum oxidation during

the deposition.

3.1.5 Lift-off and wet etching

After the e-beam deposition of the aluminum films, unwanted aluminum remains on top of the photoresist. To remove the aluminum/photoresist layer, the samples are immersed in acetone with the aluminum side facing downwards for at least an hour. The photoresist dissolves in acetone and gravity pulls the unwanted aluminum off as shown in Figure 3.4. Then the samples rinsed with clean acetone to remove most of the aluminum/photoresist layer. Follow this the sample is immersed in acetone again for a 4 minutes ultrasonic bath to remove the small piece of remaining aluminum/photoresist layer. The lift-off process requires adding a photoresist layer

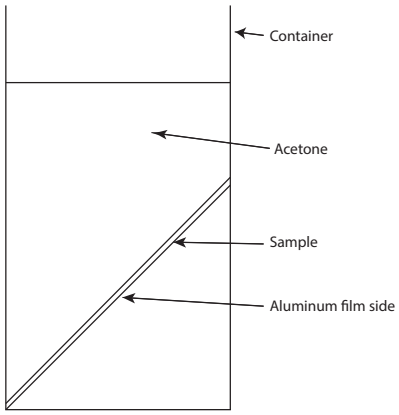

Figure 3.4: Schematic of lift-off process

before depositing the aluminum films, which might resulting in bad adhesion of the aluminum layer to the substrate. Aluminum wet etching has also been tried to produce the heaters. An aluminum film with thickness of 180 nm is directly deposited to the surface of the sample by e-beam deposition. Then the heater

pattern is generated by photolithography using the recipe discussed above with several modifications. After the developing, the samples are hard-baked on a 115 °C hot plate for 4 minutes. For longer hard bake time, the photoresist can hold up longer against the aluminum etchant. The aluminum is slightly more reflective than the insulation layer, thus the exposure time for the aluminum etching process should also be slightly shorter. The exposure time and developing time used for the wet etching process is 15 seconds and 68 seconds respectively. The exposure time of the wet etching process is shorter than the exposure time for the lift-off process, and the reason for that is basically the mask for the wet etching is in the center area of the exposure window while the mask for the lift-off process is off the center where the exposure power is dramatically dropped.

3.2 3ω Measurements

In this section, the circuitry and instruments used in the 3ω measurements are discussed in detail. The 3ω measurement system is build by River Wiedle and Mark Warner and has been demonstrated to be capable of measuring thermal conductivity of bulk and thin film dielectrics [21]. Since the 3ω signal from the amorphous metal films is smaller than that from the dielectric films, the system has been carefully calibrated and improved to extend the capability to measure thermal conductivity of amorphous metals.

3.2.1 Circuitry

Figure 3.5 shows the schematic of circuits used in the 3ω measurement system. The heater is connected in series with a adjustable matching resistor and a 1Ω resistor through the current contact pads and the whole chain of resistors is driven by a 1ω AC voltage generated by the internal function generator of the lock-in amplifier. Three instrumentation amplifiers (INA128 obtained from Texas Instruments) are used to probe and isolates the third harmonic voltage as well as 1ω voltage and 1ω current. Amplifier C in figure 3.5 has a unity gain and is used to sense the 1ω

current through the heater. Amplifier B in figure 3.5 also has a unity gain and is used to obtain the oscillating voltage from the voltage contact pads which contains both 1ω and 3ω components. Amplifier A has a adjustable gain and is used to produce a signal including only 1ω part. The matching resistor and amplifier A are adjusted together to obtain such a 1ω voltage that matches with the 1ω part across the heater. The $V_{1\omega}$ and $I_{1\omega}$ signals obtained from amplifier B and C are displayed in Agilent DSO-X 2002A oscilloscope and their RMS values are measured by Keithley 195A and Tektronix DM 5120 digital multimeters respectively. Both signals from amplifier B and A are fed into the lock-in amplifier which extracts the third harmonic voltage, also displayed on a Tektronix 2205 oscilloscope. The lock-in amplifier is SR850 from Standford Research Systems with a bandwidth range from 1 mHz to 102.4 KHz (3ω), so that the maximal possible driving frequency is about 34 KHz (1ω).

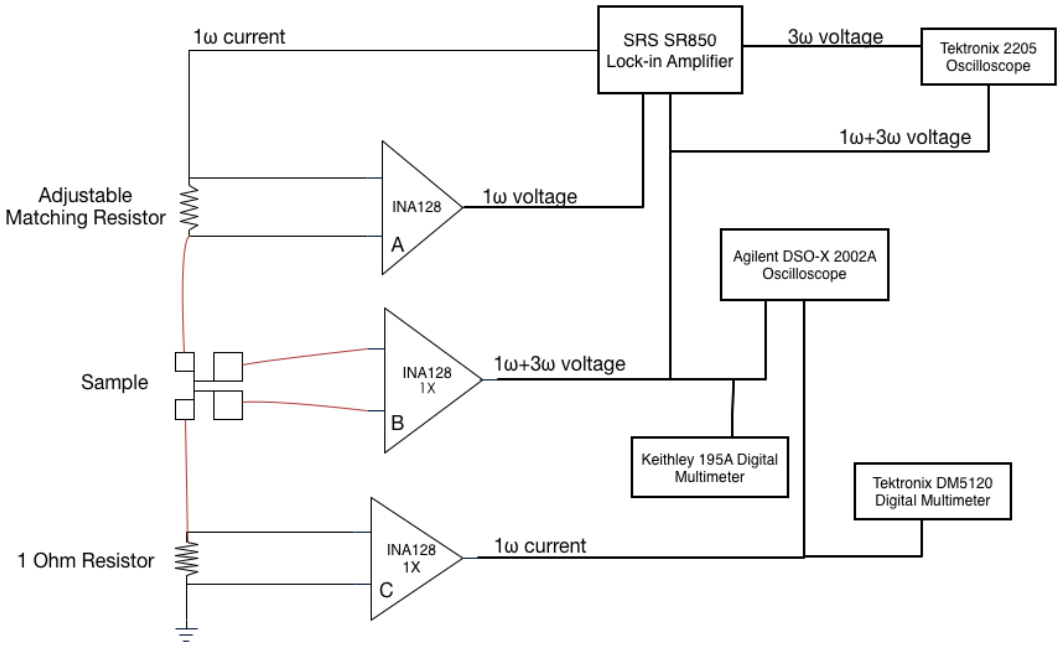

Figure 3.5: Schematic of circuits used in 3ω measurement system

3.2.2 Procedure

A set of pogo pins pushed down to the contact pads connects the heater into the 3ω measurement system. The amplitude of the voltage generated by the lock-in amplifier is set as 5 Vrms with a 50 Ω output impedance. And the effective voltage across the heater varies with the resistance of the heater. The frequency response of the in-phase and out-of-phase components of 3ω voltage as well as the 1ω voltage and 1ω current are measured and plotted using a LabVIEW program. Before taking automated measurements, the system especially the lock-in amplifier needs to be configured as following:

1. The resistance of the matching resistor is adjusted to maximum value below the sample resistance. Then the gain of amplifier B is adjusted to cancel out all the 1ω part.
2. "Coupling" from the "INPUT FILERS" menu is set to "DC"; "Time Constant" from the "GAIN TC" menu is set to "3 seconds"; "Filter" from "GAIN TC" menu is set to "24 dB/oct"; "Reserve" from the "GAIN TC" menu is set to "MAX".
3. To find out the reference phase for the third harmonic voltage. The initial phase ϕ_0 of the driving voltage is determined: "Harmonic" from the "REF PHASE" menu is set to "1", "Source" from the "INPUTER FILTERS" menu is set to "A", "Sensitivity" from the "GAIN TC" is set to minimum value, then the out-of-phase component of 1ω voltage is set zero by pressing the "AUTO PHASE" button. Secondly the reference phase for the third harmonic voltage is set to three times its displayed value according to equation 2.5. Finally, the "Harmonic" from "REF PHASE" menu is set back to "3", the "Source" from the "INPUTER FILTERS" menu is set to "A-B", the "Sensitivity" from the "GAIN TC" menu is set to its possible maximum value such that maximum measured voltage is still in the range.

The LabVIEW program also includes a signal stabilization routine which can ensure the locked 3ω signals have actually settled before the data points are recorded.

3.2.3 Temperature coefficient of resistance (TCR) measurements

Temperature coefficient of resistance (TCR) is a critical parameter in the 3ω measurements because it converts the measured 3ω voltage to a oscillating temperature rise from which the thermal properties of substrates and thin films. TCR of deposited metal films depends heavily on the deposition process and can be quite different from the bulk values and must be experimentally determined. For the TCR measurements, the same circuitry are used and a small K-type chromel-alumel thermocouple is attached to the surface of the samples by nail polish at a position close to the heater. The substrate is placed on top of a cooper block with one high-ohmic heater embedded in the block. During the TCR measurements, the samples are heated up from room temperature to about 10 degrees above the room temperature. A portable thermocouple to analog connector is used converting signal measured by the thermocouple to analog signals that can measured and recorded by the digital multimeter. Data points are taken with 0.3°C-steps while the cooper block is heated up, including the temperature of the heater measured by the thermocouple mounted close to the heater, the RMS voltage and RMS current of the heater measured by Keithley 195A and Tektronix DM 5120 digital multimeter respectively. The resistance of the heater is calculated from measured RMS current and RMS voltage. Then the temperature coefficient of resistance is determined from:

$$\alpha = \frac{1}{R_0}\frac{dR(T)}{dT}$$

where R_0 is the resistance of the heater during the 3ω measurements and $\frac{dR(T)}{dT}$ is the slope of the linear fitted line of resistances to temperatures.

3.2.4 Improvements to the measurements of 1ω voltage and 1ω current

The previous set-up of 3ω measurement system has a big inaccuracy issue in RMS 1ω voltage and 1ω current measurements. The effective 1ω voltage and 1ω current across the heater depends on the resistance of the heater but doesn't depend on the frequency of the driving current, suggesting that the magnitude of $V_{1\omega}$ and $I_{1\omega}$ should remains constant for one heater regardless of the driving frequency. As figure 3.6(a) and figure 3.6(b) showed, our previous measured RMS $V_{1\omega}$ and $I_{1\omega}$ is very fluctuated respect to frequency and the deviation is much larger than the order of electrical noise. $V_{1\omega}$ and $I_{1\omega}$ are both important parameters needed in converting 3ω voltage to thermal resistance and to determine the thermal conductivities. The thermal resistance calculated using the fluctuated $V_{1\omega}$ and $I_{1\omega}$ is very problematic and shows no trend respect to frequency as expected. The average of $V_{1\omega}$ and $I_{1\omega}$ are used in previous measurement as alternatives. To address whether the 3ω method fails for certain materials or our system is not capable of measuring $V_{1\omega}$ and $I_{1\omega}$ accurately, efforts has been made to diagnose and calibrate the 3ω measurement system. And the cause of the issue turns out to be extremely simple. Previously the Agilent DSO-X 2002A oscilloscope is programmed to measure the RMS $V_{1\omega}$ and RMS $I_{1\omega}$ and it has two modes for calculating the RMS amplitude of the input signal. One determine the RMS amplitude using one period of the waveform while the other one used the full-screen waveform. As the frequency of driving current changes, the portion of the full-screen waveform is different thus the calculated RMS amplitude can be dramatically fluctuated. Figure 3.6(a) and figure 3.6(b) also showed the RMS $V_{1\omega}$ and RMS $I_{1\omega}$ measured by the oscilloscope using only one cycle of the waveform. Moreover, two more accurate digital multimeter Keithley 195A and Tektronix DM 5120 have been added to the system for accurately measurements of the RMS $V_{1\omega}$ and $I_{1\omega}$ of the heater. Clearly we can see that the standard deviation of $V_{1\omega}$ and $I_{1\omega}$ drops below 0.1% after the instrumental improvements. And in Chapter 4, we will also show that the fluctuation of the $V_{1\omega}$ after the instrumental improvements is negligible in calculating the thermal

conductivity of thin-film TaWSi.

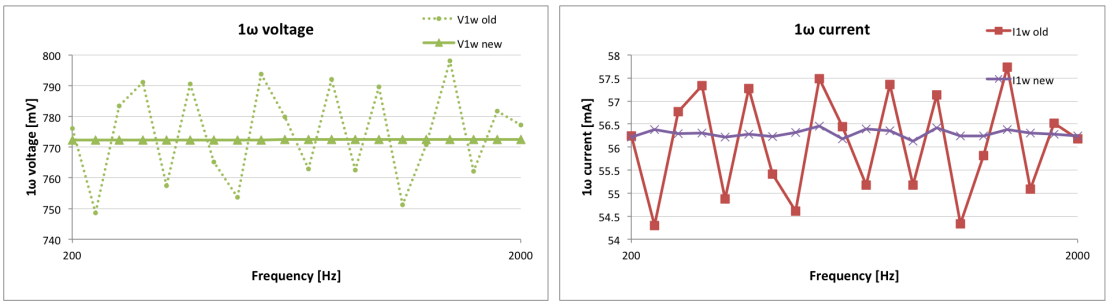

(a) Fluctuation in $V_{1\omega}$ at different frequency (b) Fluctuation in $I_{1\omega}$ at different frequency

Figure 3.6: (a) Data labeled with "$V_{1\omega}$ old" and "$V_{1\omega}$ new"show the fluctuation of 1ω voltage before and after the instrumental improvements respectively; (b) Data labeled with "$I_{1\omega}$ old" and "$I_{1\omega}$ new"show the fluctuation of 1ω current before and after the instrumental improvements respectively.

3.2.5 Probe stage with the micromanipulator

Micromanipulators have been added to the 3ω measurement system to improve the reproducibly of the measurements and to improve the accuracy of the TCR measurements. It is very tricky and difficult to properly connected the samples into the measurement circuit using the pogo pins and the set up as showed in figure 3.7.

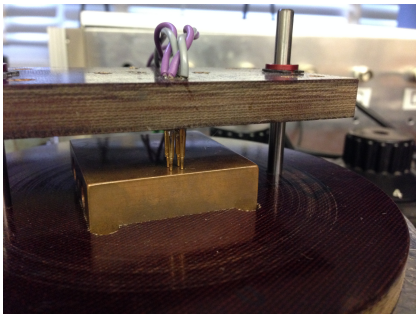

Figure 3.7: Side view of pogo pins and set-up for connecting the sample into the 3ω measurement system.

The position where the pogo pins pushed down to the contact pads and the amount of force that the pogo pins applied to the aluminum films are both uncontrollable. Figure 3.8 shows the image of the contact pads after the 3ω measurements. For this particular heater, it becomes much more difficult to make

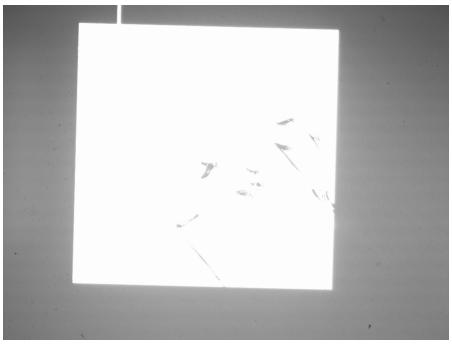

Figure 3.8: Image of the voltage contact pad of a heater after several measurements under 5X microscopy

good connection between the samples and the pogo pins and the measured data can be problematic. It is also very difficult to mount a thermocouple as close as possible to the heater during the TCR measurements. As we can see in figure 3.9, sometimes the temperature measured by the attached thermocouple can also be different from the actual temperature of the heater because the thermocouple is blocked by the pogo pins and can not be mounted sufficient close to the heater.

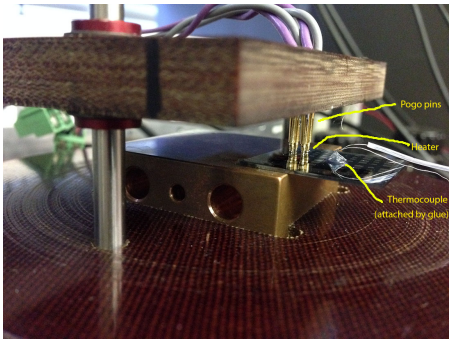

Figure 3.9: Example of thermocouple mounted to area far away from the heater.

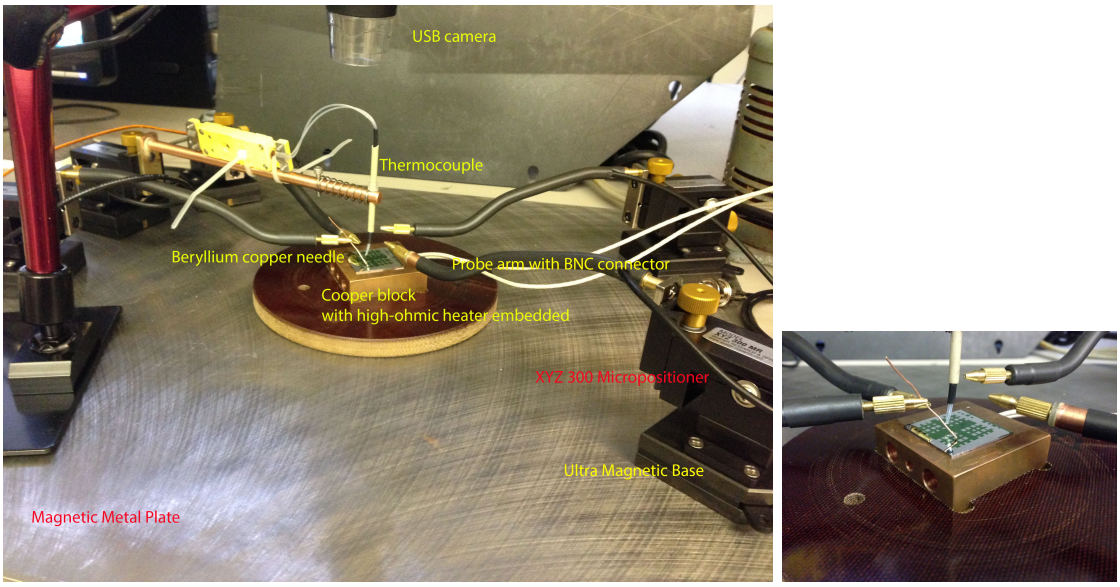

(a) probe stage (b) zoom out view

Figure 3.10: (a) Image of probe stage with five XYZ 300 micropositioner; (b) Zoom out view of the sample holder and probes.

Figure 3.10(a) and figure 3.10(b) shows the schematic of the probe stage that will be added to the 3ω measurement system. The base is a magnetic metal plate. Four XYZ 300 micropositioner from Quater-Research are used to move probes to the four contact pads of the heater. One XYZ 300 micropositioner are used to mount the thermocouple. Figure 3.11 shows how the thermocouple is mounted to the micropositioner (build by Mark Warner). With this set-up, the thermocouple can be mounted very close to the heater and without using any glue or nail polish. Beryllium copper needles instead of tungsten needles are used as the probes. The signal obtained from the beryllium copper needles can be directed output to the instruments with BNC connector.

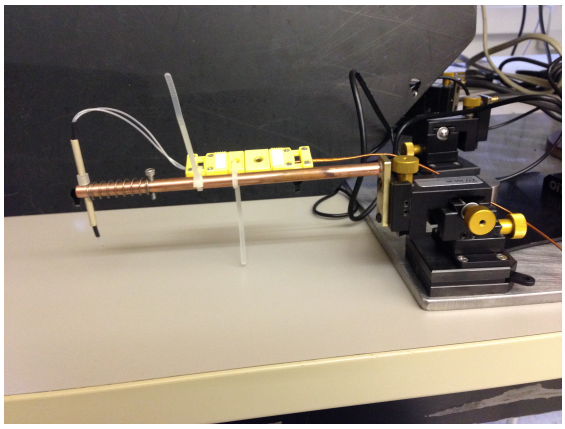

Figure 3.11: Image of the thermocouple probe controlled by a XYZ 300 micropositioner.

The temperature obtained from the thermocouple is feed back to a Omega programmable temperature controller which controls the heating current of the high-ohmic heater that embed inside the copper block. Thus the temperature can be accurately controlled during the TCR measurements.

Chapter 4: Results

4.1 Thermal conductivity measurements of hafnium oxide

24.4 nm, 60 nm, and 80 nm thickness of hafnium oxide thin film are deposited on top of p-type silicon substrate with 100 nm thickness thermal oxide (SiO_2) by atomic layer deposition at HP. The aluminum heater with a thickness of 180 nm was deposited by e-beam deposition in the Owen cleanroom. The length of heaters is 1 mm while the width of heaters can be 5 μm, 10 μm, 15 μm, 20 μm. The thermal resistance increase caused by the hafnium oxide thin film does not depend on the width of heaters. From Equation 2.42, by choosing a heater with smaller width, the magnitude of third harmonic $V_{3\omega}$ is larger, which will be easier to discern and measured by the lock-in amplifier. The 5 μm heaters can be easily destroyed during lift-off process and the roughness of 5 μm heaters is relatively more significant for other heaters. Thus the most reliable results come from $V_{3\omega}$ measurements and TCR measurements on 10 μm heaters. The reason for choosing same width heaters from different samples is to minimize any possible variations caused by the size difference of heaters, including the variations of TCR.

4.1.1 Temperature coefficient of resistance

The temperature coefficient of resistance (TCR) α is an important parameter to determine the thermal conductivity of both the substrate and hafnium oxide. Because the variation of TCR depends on the thin film geometry, the value of TCR of the aluminum heater cannot be looked up in literature and we need to experimentally determine the TCR value.

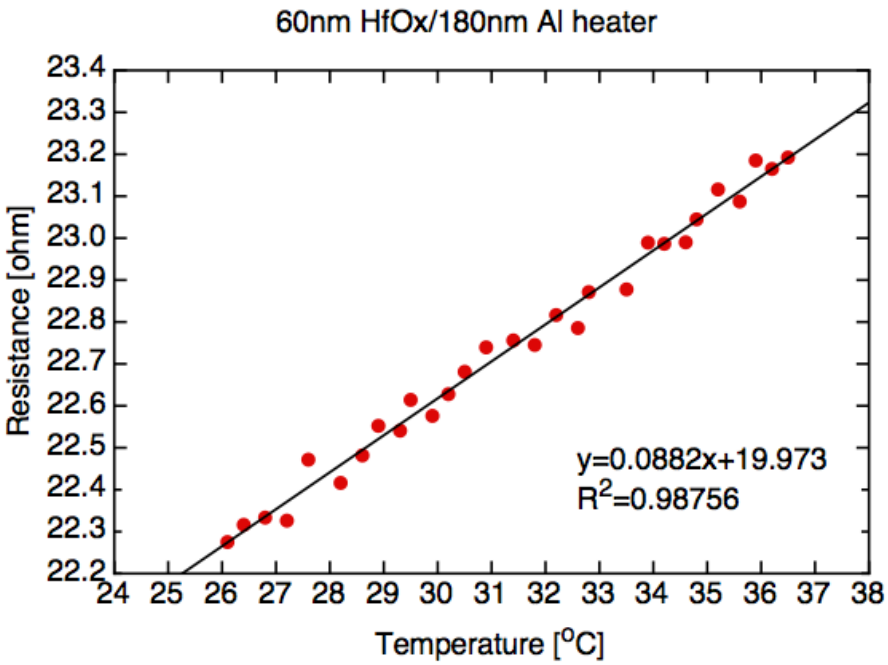

Figure 4.1: Resistance R of heater in dependence of temperature T. Resistance during 3ω measurement is 22.2 Ω. Temperature coefficient of resistance is 0.00397 K^{-1}.

Figure 4.1 shows the resistance R of a heater as a function of temperature. The heater was picked from 60 nm HfOx sample. The geometry of heater is 1 mm in length, 7.86 μm in width and 180 nm in thickness. The width was measured by microscopy under 150×-amplification. The sample was put on top of a copper stage. A small K-type-chromel-alumel thermocouple was mounted on the surface of the sample close to the heater (approximately 3 mm distance) to determine the temperature of the heater. While the sample was heated up by the copper stage, the V_{rms} and I_{rms} was measured every 0.3 °C from 26 °C to 37 °C. Linear fitting of the data points gives the slope $\frac{dR}{dT}$=0.0882 $\frac{\Omega}{K}$ with an fraction error of 2.2%. Using the resistance during $V_{3\omega}$ measurements R_0, the TCR is

$$\alpha = \frac{1}{R_0}\frac{dR}{dT} = \frac{0.0882}{22.2} = 0.00397K^{-1}$$

4.1.2 3ω voltage and thermal conductivity of substrate

Figure 4.2 shows the in-phase and out-of-phase components of 3ω voltage. The data come from measurement on a 10 μm heater on 80 nm HfOx sample. The in-phase component $V_{3\omega,x}$ is linearly proportional to the driving frequency in log scale. While the out-of-phase component is almost constant at the frequency range of 200 Hz to 2000 Hz. Using Equation 2.43, The inverse slope gives the thermal conductivity of p-type silicon substrate as 153 $Wm^{-1}K^{-1}$ with total fraction error of 6.8%. Our measured value lies in the range of thermal conductivity of p-type silicon substrate as reported in literatures [16, 48].

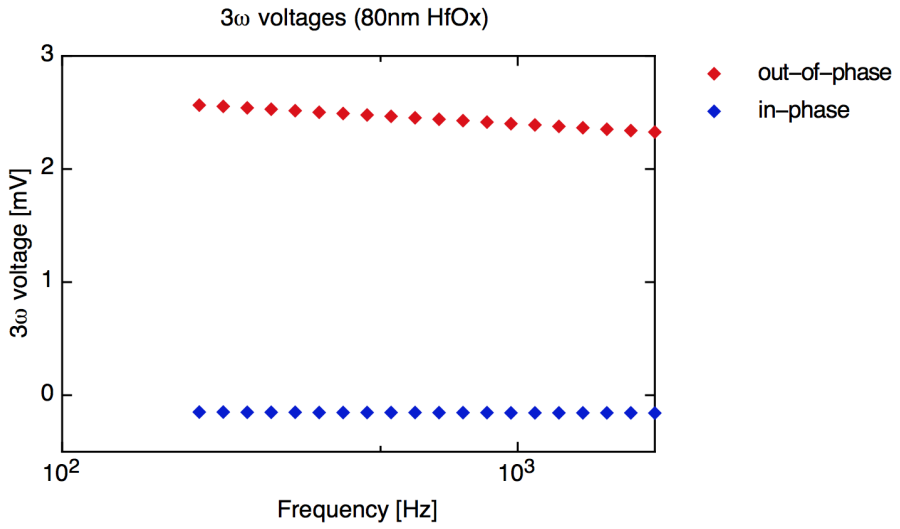

Figure 4.2: In-phase and out-of-phase components of 3ω voltage. The inverse slope gives the thermal conductivity of p-Si as 153 $Wm^{-1}K^{-1}$ with total fractional error of 6.8%.

4.1.3 Thermal conductivity of thin-film hafnium oxide

Figure 4.3 shows the in-phase thermal resistance vs. driving frequency for hafnium oxide samples with different thickness. Measurements was conducted on two different $10\mu m$ width heaters for each thickness. Figure 4.4 plots the average in-phase

thermal resistance vs. the film thickness of HfOx. As expected, the addition of a HfOx thin film only adds a frequency independent in-phase thermal resistance increase. Based on Equation 2.47, the thermal conductivity of hafnium oxide thin film is 0.78 ($\pm$0.05) $Wm^{-1}K^{-1}$. The intercept $\Delta R_i = 87.2m^2KGW^{-1}$ is the contribution of thermal resistance presented at the interface of substrate-film and film-heater.

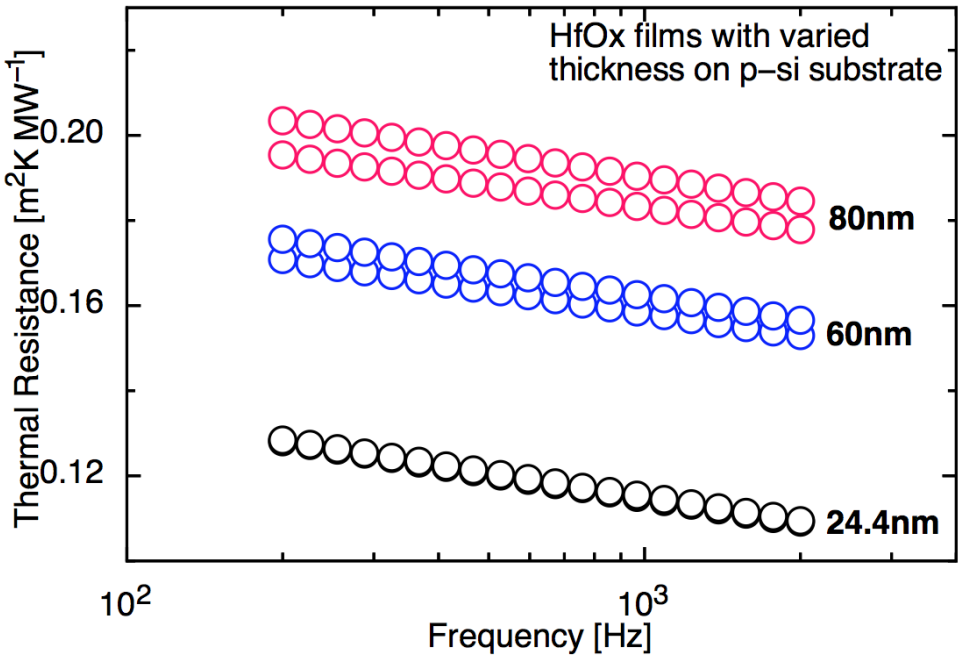

Figure 4.3: Thermal resistance vs. driving frequency for a series of HfOx films on p-type silicon.

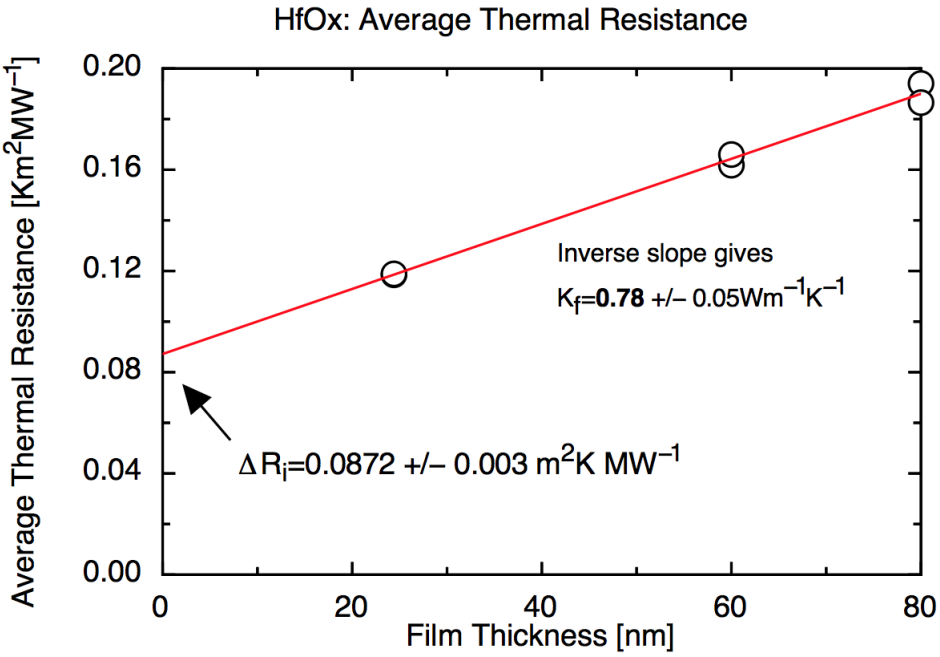

Figure 4.4: Average thermal resistance vs. d_f for a series of HfOx films on p-type silicon.

Panzer et al. [49] reports a thickness dependent room-temperature intrinsic thermal conductivity of thin-film HfO_2 as 0.49 to 0.95 $Wm^{-1}K^{-1}$ for films of thickness from 5.6 to 20 nm. The intrinsic HfO_2 thermal conductivity depends on the film thickness and post-deposition processing, deviating from both bulk values and the measurements of effective film thermal conductivities.

Table 4.1: Results: thermal conductivity of hafnium oxide films

sample	width of heater	thermal conductivity $[Wm^{-1}K^{-1}]$
HfO_2	10 μm heater	0.78±0.05

4.2 Thermal conductivity measurements of amorphous metal thin film TaWSi

TaWSi films of thickness 200 nm, 250 nm, 300 nm and 350 nm were deposited on p-type silicon substrate with 100 nm thermal oxide (SiO_2) by DC magnetron sputtering at Hewlett Packard Laboratory (HP). Then a thin layer of hafnium oxide was deposited on top of the TaWSi films by atomic layer deposition at HP, providing insulation between the aluminum heater and the TaWSi films. Four different thicknesses (24.4 nm, 40 nm, 60 nm, 80 nm) of HfOx were tried to find out sufficient thickness for the insulation layer. The aluminum heater with a thickness of 180 nm was deposited by e-beam deposition in the cleanroom facility in Owen Hall at Oregon State University. The results are summarized in Table 4.2, which shows that the 80-nm HfO_2 was optimum. The 40-nm HfO_2 layer gave consistent results, but we suspect a labeling error in this experiment, so results must be treated with caution. The 24.4-nm HfO_2 proved too thin and breakthrough occurred. The results are presented separately in the following sections.

Table 4.2: Results: thermal conductivity of amorphous TaWSi films

sample	insulation layer	width of heater	thermal conductivity $[Wm^{-1}K^{-1}]$
TaWSi	80 nm HfO_2	10 μm heater	2.39±0.27
TaWSi	80 nm HfO_2	15 μm heater	2.40±0.40
TaWSi	80 nm HfO_2	20 μm heater	2.85±0.60
TaWSi	40 nm HfO_2	10 μm heater	2.93±0.30[a]
TaWSi	24.4 nm HfO_2	10 μm heater	2.14±0.22[b]

[a] possible mislabeling [inconclusive result] [b] heater easily get breakthrough

4.2.1 Thin-film TaWSi samples with 80 nm of HfOx insulation layer

The most reliable results were obtained from $V_{3\omega}$ measurements and TCR measurements on 10 μm heaters. Measurements were conducted on 15 μm and 20 μm

heaters for comparison.

4.2.1.1 Temperature coefficient of resistance

Figure 4.5 shows the resistance R of a heater in dependence of temperature. The heater was picked from 250 nm TaWSi sample. The geometry of heater is 1 mm in length, 17.1 μm in width and 180 nm in thickness. The width was measured by microscopy under 150×-amplification. The sample was put on top of a copper stage. A small K-type-chromel-alumel thermocouple was mounted on the surface of the sample close to the heater (approximately 3 mm distance) to determine the temperature of the heater. While the sample was heated up by the copper stage, the V_{rms} and I_{rms} was measured every 0.3 °C from 23 °C to 35 °C. Linear fitting of the data points gives the slope $\frac{dR}{dT}$=0.0408 $\frac{\Omega}{K}$ with an fraction error of 0.4%.

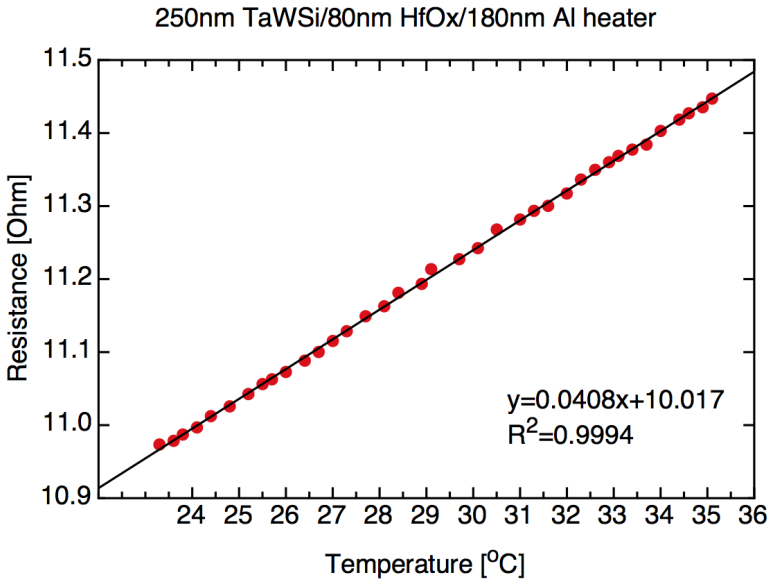

Figure 4.5: Resistance R of heater in dependence of temperature T. Heater resistance during 3ω measurements is 10.98 Ω. Temperature coefficient of resistance is 0.00371 K^{-1}.

Using the resistance during $V_{3\omega}$ measurements R_0, the TCR is

$$\alpha = \frac{1}{R_0}\frac{dR}{dT} = \frac{0.0408}{10.98} = 0.00371K^{-1} \tag{4.1}$$

The value obtained here is slightly smaller than previous measurements. The fraction error in linear-fitted slope is much smaller. This is a result of bring in two new digital meters for more accurate measurements of V_{rms} and I_{rms}.

4.2.1.2 3ω voltage and thermal conductivity of substrate

Figure 4.6 shows the in-phase and out-of-phase components of the 3ω voltage.

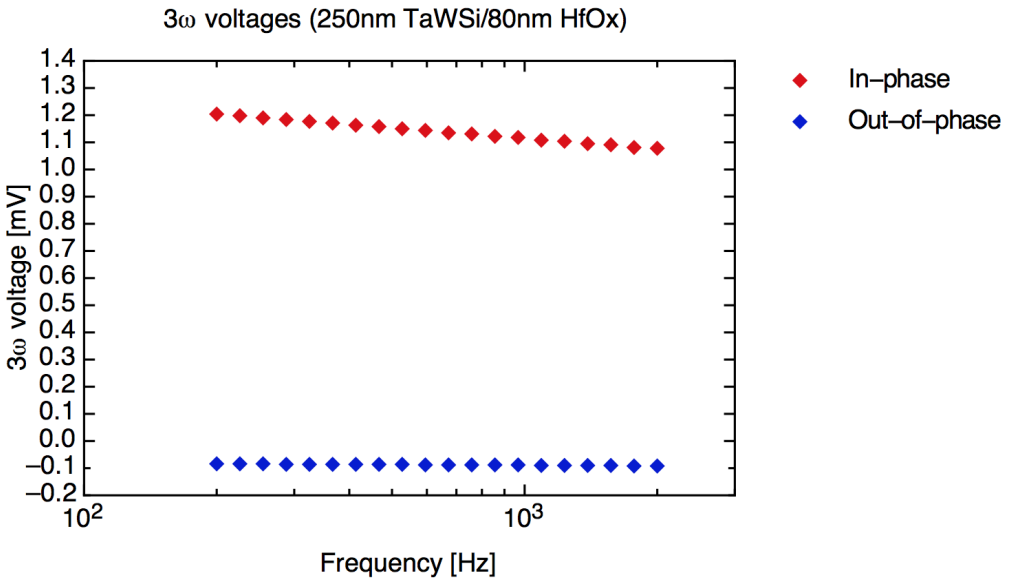

Figure 4.6: In-phase and out-of-phase components of 3ω voltage. The inverse slope gives thermal conductivity of p-Si substrate as 150.7 $Wm^{-1}K^{-1}$ with total fractional error 3.4%.

The data come from measurement on a 17.1 μm heater on a 250 nm TaWSi sample with an 80 nm HfOx insulation layer. The in-phase component $V_{3\omega,x}$ is linearly proportion to the driving frequency log scale. The slope can be used to calculate

the thermal conductivity of the p-type silicon substrate as 150.7 $Wm^{-1}K^{-1}$ with total fractional error of 3.4%. This value is consistent with previous measurements on HfOx samples and TaWSi samples with 40 nm HfOx.

4.2.1.3 Thermal conductivity of thin-film TaWSi; measurements on 10 μm heaters

Figure 4.7 shows the in-phase thermal resistance vs. driving frequency for TaWSi samples with different thicknesses. Previously measured data for 80 nm HfOx sample (no TaWSi) is also plotted here as reference. Measurements were conducted on 10μm width heaters for each thickness. Figure 4.8 plots the average in-phase thermal resistance vs. the film thickness of TaWSi. The previously measured data for 80 nm HfOx is plotted as zero thickness of TaWSi. As expected, the addition of a TaWSi thin film only adds a frequency independent in-phase thermal resistance. Based on Equation 2.47, the thermal conductivity of TaWSi thin film is 2.39 ($\pm$0.27) $Wm^{-1}K^{-1}$. The linear fit here was based on all the five data points, including reference data point of 80 nm HfOx samples. The error bar in figure 4.8 includes the statistical error of $V_{1\omega}$, and $I_{1\omega}$, as well as the standard deviation of width and length of the heater used in measurements. The error thermal conductivity contains the error in linear regression with error bar as well as the systematic error TCR.

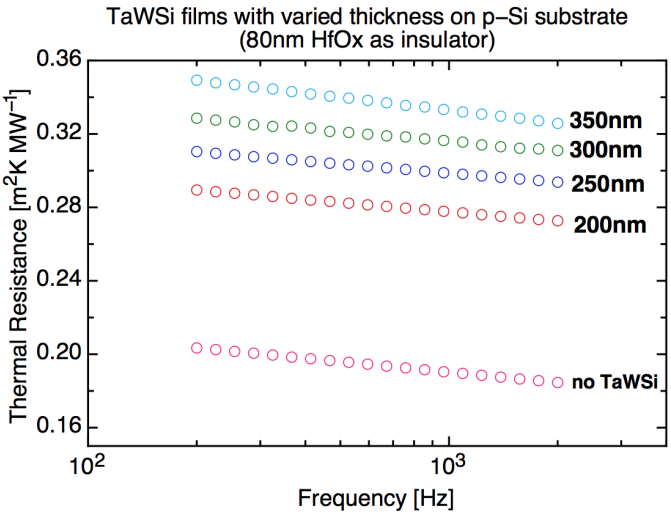

Figure 4.7: Thermal resistance vs. driving frequency for a series of TaWSi films on p-type silicon with 80 nm HfOx. Previous measured data for 80 nm HfOx is also plotted here as reference.

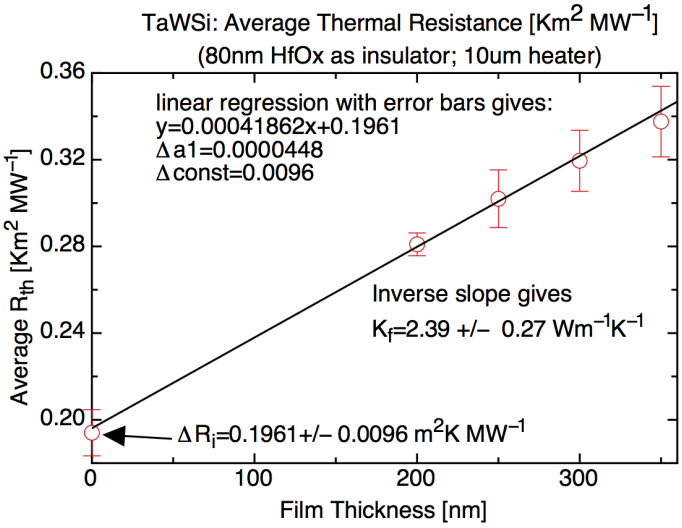

Figure 4.8: Average thermal resistance vs. d_f for a series of TaWSi films on p-type silicon with 80 nm HfOx.

4.2.1.4 The influence of the $V_{1\omega}$ and $I_{1\omega}$ fluctuations

According to Equation 2.42, an accurate ac root mean square voltage measurement is essential for converting the 3ω voltage to thermal resistance. We improved the system by adding two new digital meters with higher accuracy (Keithley 195A and Tektronix DM5120 in Figure 3.5). As we know that

$$R_{th} = \frac{\Delta T_{AC}}{Q}$$

where $Q = \frac{V_{1\omega} I_{1\omega}}{2bl}$. $V_{1\omega}$ and $I_{1\omega}$ are assume constant during each measurement regardless of the driving frequency, but in practice fluctuate due to electrical noise. The typical standard deviation of Q during each measurement is about 0.1%. Figure 4.9 and figure 4.10 plot the thermal resistance increase for a series of TaWSi films with various film thickness at different driving frequencies. Figure 4.9 use measured Q in converting $V_{3\omega}$ to temperature rise ΔT_{AC}. Figure 4.9 shows the fluctuations in ΔR_{th} at different frequency due to the electrical noise of $V_{1\omega}$ and $I_{1\omega}$. While in figure 4.10, average Q is used for converting the third harmonic voltage $V_{3\omega}$ to temperature rise ΔT_{AC}.

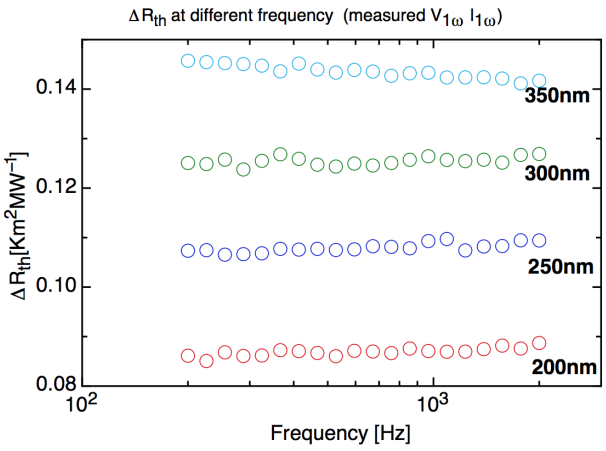

Figure 4.9: Thermal resistance offset ΔR_{th} vs. driving frequency for a series of TaWSi films; Measured Q is used to convert $V_{3\omega}$ to temperature rise ΔT_{AC}.

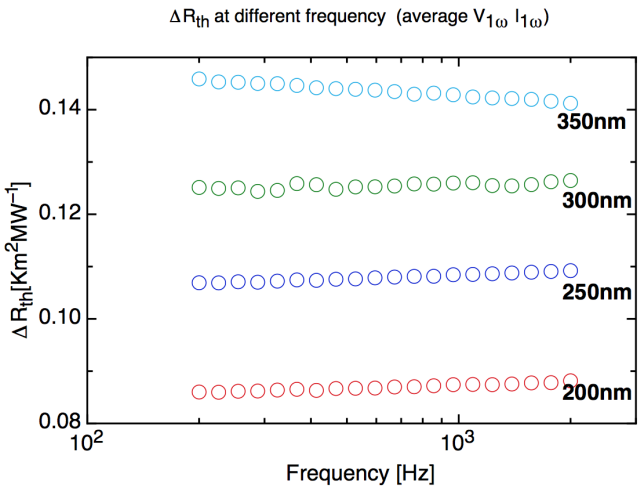

Figure 4.10: Thermal resistance increase ΔR_{th} vs. driving frequency for a series of TaWSi films; Average Q is used to convert $V_{3\omega}$ to temperature rise ΔT_{AC}.

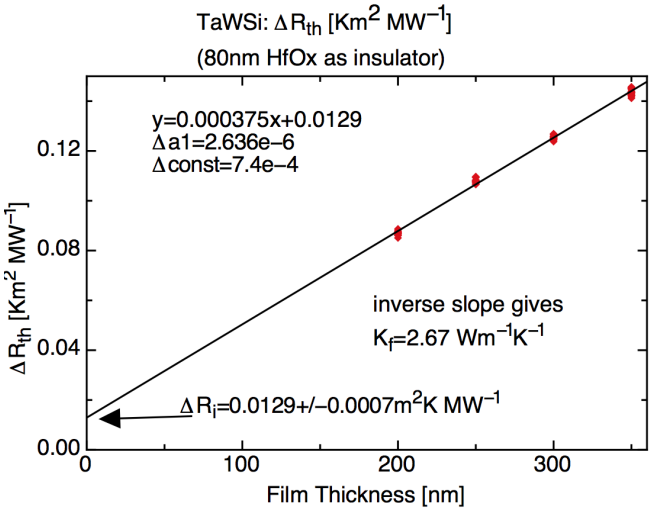

Figure 4.11: Thermal resistance increase ΔR_{th} vs. d_f for a series of TaWSi films on p-type silicon with 80 nm HfOx. Measured Q is used to convert $V_{3\omega}$ to temperature rise ΔT_{AC}.

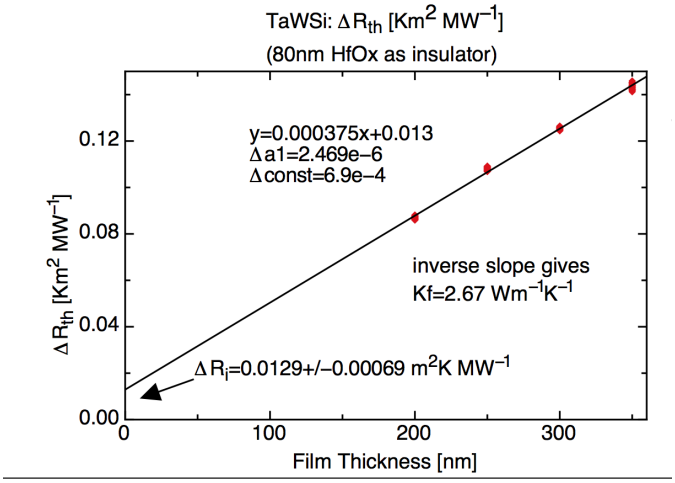

Figure 4.12: Thermal resistance increase ΔR_{th} vs. d_f for a series of TaWSi films on p-type silicon with 80 nm HfOx. Average Q is used to convert $V_{3\omega}$ to temperature rise ΔT_{AC}.

Figure 4.11 and figure 4.12 plot the thermal resistance increase ΔR_{th} vs. the film thickness d_f for a series of TaWSi films. ΔR_{th} obtained from calculating thermal resistance offset at different frequency were plotted in the same graphs. Figure 4.11 use the measured heat flux Q in converting $V_{3\omega}$ to temperature rise ΔT_{AC} while figure 4.12 use the average Q. The linear fit of data points in figure 4.11 and figure 4.12 both yields the thermal conductivity of TaWSi as 2.67 $Wm^{-1}K^{-1}$. The linear fit here was based on four data points, not including reference data point of 80 nm HfOx samples. Figure 4.11 and figure 4.12 also suggest that the electrical noise in $V_{1\omega}$ and $I_{1\omega}$ is too small to cause a discernible error in calculating the thermal conductivity of thin-film TaWSi. The intercept $\Delta R_i = 0.0129\ m^2KMW^{-1}$ is the contribution of thermal resistance presented at the interface of SiO_2/TaWSi and TaWSi/HfOx, subtracting the contribution of thermal resistance presented at the interface of SiO_2/HfOx.

4.2.1.5 TCR measurements on multiple heaters

Typically, the temperature coefficient of resistance (TCR) of thin-film aluminum is smaller than the value of bulk aluminum (0.00429 K^{-1}) and it may depend on deposition conditions[reference]. We measured the TCR of multiple heaters with 10 μm, 15 μm and 20 μm width on various TaWSi samples with different thicknesses. The largest value is 0.00445 K^{-1} and the smallest value is 0.00360 K^{-1}. The TCR of the 300 nm TaWSi sample was larger than the TCR of bulk aluminum, which suggests that there is a significant error in the measurement of a particular TCR. According to Equation 2.42, the thermal resistance is described as

$$R_{th} = \frac{4bl}{V_{1\omega}^2 I_{1\omega}} \frac{1}{\alpha} V_{3\omega,x}$$

The TCR α is important in converting the in-phase 3ω voltage to thermal resistance R_{th}. In figure 4.13 we plot the average thermal resistance vs. d_f for a series of TaWSi films on p-type silicon. The TCR measured for the particular heater is used to convert the third harmonic voltage to thermal resistance. These plots do not show consistent linear relation between the average thermal resistance and the film thickness. The situation is improved if we use the average TCR for all heaters of the same width (excluding the anomalously large TCR of the 300 nm sample) to calculate the thermal resistance and this is shown in Figure 4.14 for the same data as in Figure 4.13. Now the average thermal resistance shows the expected linear relation to thickness and there is an systematic offset between thermal resistances measured from heaters with different width. The reasons for the offset may came from the different contributions of thermal resistance presented at the interface between HfOx insulation layer and heaters of different width. Another possible reason is that as the width of heaters increase, the magnitude of third harmonic decreases, making it more difficult to discern and measuring the $V_{3\omega}$. Thus as the width of heater increases, the error of thermal resistance is greater and that may account for the offset we see in figure 4.14.

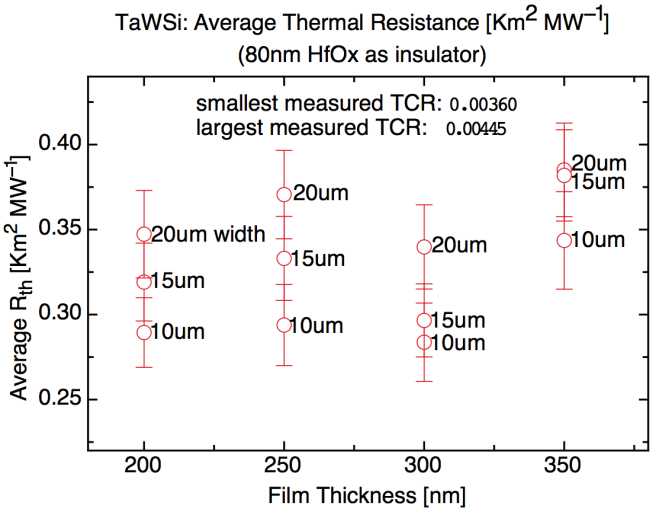

Figure 4.13: Average thermal resistance vs. d_f for a series of TaWSi films on p-type silicon with 80 nm HfOx. Measured TCR for each particular sample is used to convert the third harmonic $V_{3\omega,x}$ to thermal resistance.

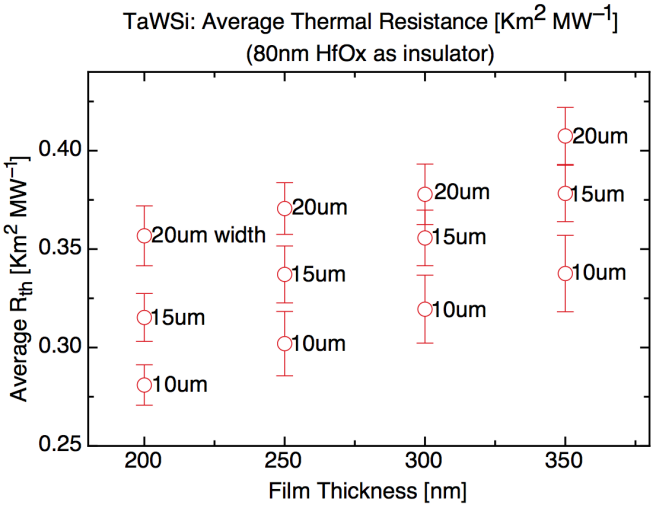

Figure 4.14: Average thermal resistance vs. d_f for a series of TaWSi films on p-type silicon with 80 nm HfOx. Average TCR for a given width is used for converting the third harmonic $V_{3\omega,x}$ to thermal resistance.

4.2.1.6 Measurements on heaters with 15 μm and 20 μm width

Figure 4.15 shows the average in-phase thermal resistance vs. the film thickness of TaWSi. Data in figure 4.15 were obtained from measurements on heaters with 15 μm width. As expected, average thermal resistance is linearly proportion to the film thickness. Based on Equation 2.47, the thermal conductivity of TaWSi thin film is 2.40 ($\pm$0.40) $Wm^{-1}K^{-1}$. The error bar in figure 4.15 includes the statistical error of $V_{1\omega}$, and $I_{1\omega}$, as well as the standard deviation of width and length of the heater used in measurements. The error in the thermal conductivity includes the error in linear regression with error bar as well as the systematic error of TCR.

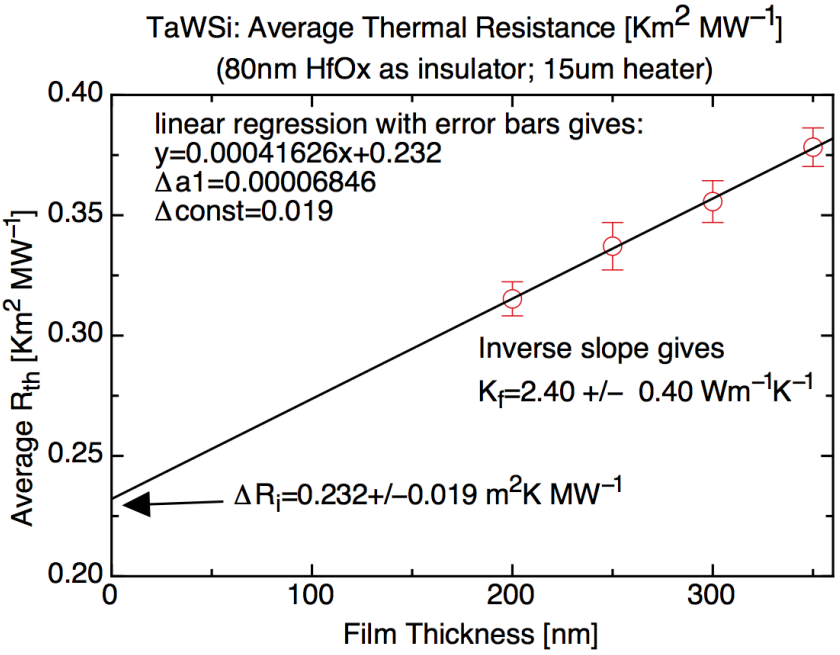

Figure 4.15: Average thermal resistance vs. d_f for a series of TaWSi films on p-type silicon. Results obtained from measurements on 15 μm width heaters.

Figure 4.16 shows the average in-phase thermal resistance vs. the film thickness of TaWSi. Data in figure 4.16 were obtained from measurements on heaters with 20 μm width. As expected, average thermal resistance is linearly proportion to the

film thickness. Based on Equation 2.41, the thermal conductivity of TaWSi thin film is 2.85 ($\pm$0.60) $Wm^{-1}K^{-1}$. The error bar in figure 4.16 includes the statistical error of $V_{1\omega}$, and $I_{1\omega}$, as well as the standard deviation of width and length of the heater used in measurements. The error of thermal conductivity including the error in linear regression with error bar as well as the systematic error of TCR.

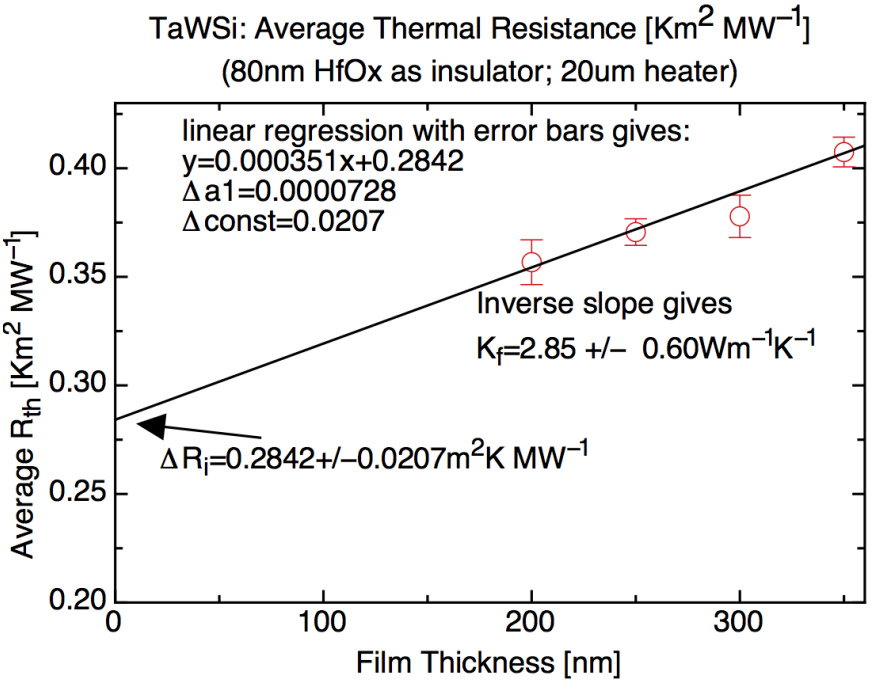

Figure 4.16: Average thermal resistance vs. d_f for a series of TaWSi films on p-type silicon. Results obtained from measurements on 20 μm width heaters.

4.2.2 Thin-film TaWSi samples with 40 nm of HfOx insulation layer(inconclusive result)

As we mentioned earlier, the 40-nm HfO_2 layer gave reasonable results, but we suspect a labeling error in this experiment. The results for this particular set of sample must be treated with caution. This inconclusive result is present here for comparison with the measurements on 24.4-nm and 80-nm HfO_2 samples. All the

results were obtained from $V_{3\omega}$ measurements and TCR measurements on 10 μm heaters.

4.2.2.1 Temperature coefficient of resistance

Figure 4.17 shows the resistance R of a heater on TaWSi samples with 40 nm HfOx in dependence of temperature. Linear fitting of the data points gives the slope $\frac{dR}{dT}$=0.0903 $\frac{\Omega}{K}$ with an fraction error of 3.2% and the resistance of heater is 22.9 Ohm. Thus the temperature of coefficient is 0.00395 K^{-1}. The TCR value measured here is consistent with previous measurements of heaters on hafnium oxide.

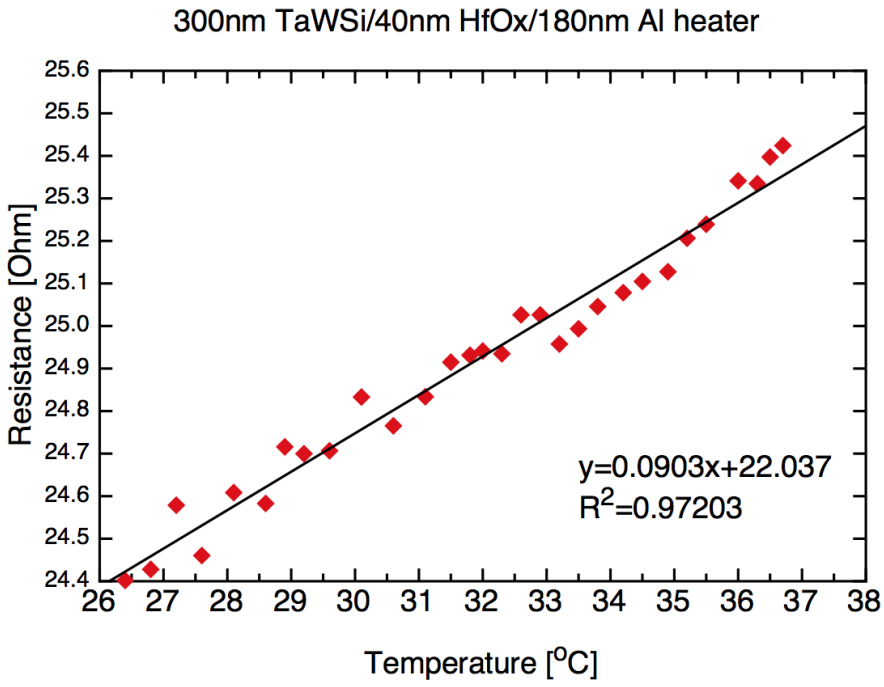

Figure 4.17: Resistance R of heater in dependence of temperature T. Heater resistance during 3ω measurement is 22.9 Ω and temperature coefficient of resistance is 0.00395 K^{-1}.

4.2.2.2 3ω voltage and thermal conductivity of substrate

Figure 4.18 shows the in-phase and out-of-phase components of 3ω voltage. The data were obtained from measurements on a 10 μm heater on 350 nm TaWSi sample with 40 nm HfOx as insulator. The inverse slope yields the thermal conductivity of p-type silicon substrate as 158 Wm^1K^1 with total fractional error of 8.7%. The values of thermal conductivity of p-type silicon measured here is consistent with previous measurements on hafnium oxide samples with the quoted error bars.

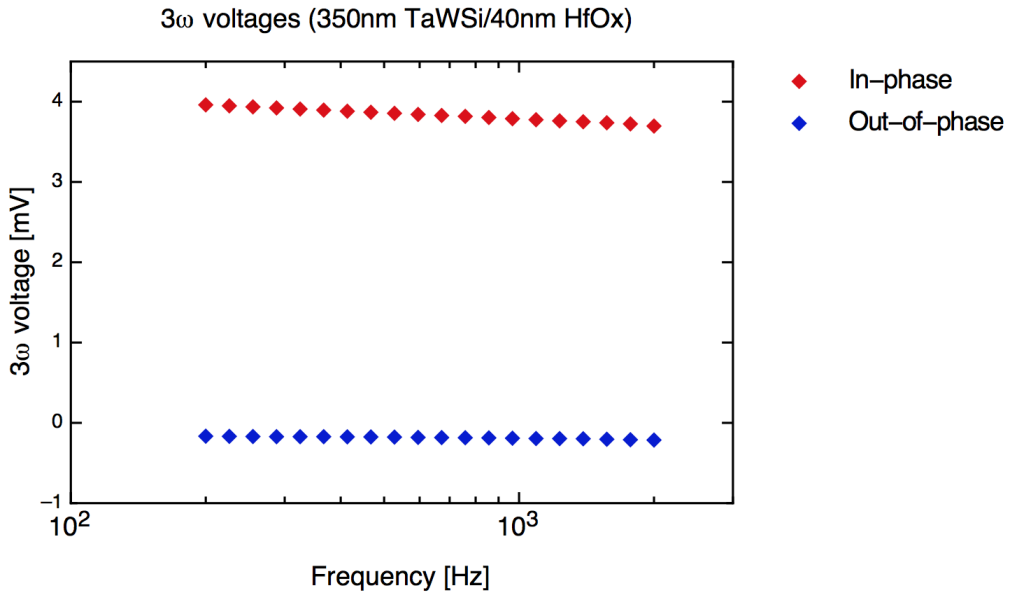

Figure 4.18: In-phase and out-of-phase components of 3ω voltage. The inverse slope gives the thermal conductivity of p-Si substrate as 158 $Wm^{-1}K^{-1}$ with total fractional error of 8.7%.

4.2.2.3 Thermal conductivity of TaWSi films

Figure 4.19 shows the in-phase thermal resistance vs. driving frequency for TaWSi samples with different thicknesses. Figure 4.20 plots the average in-phase thermal resistance vs. the film thickness of TaWSi. The results are abnormal in that the

thermal resistance rise caused by thinner TaWSi films is larger than that of thicker TaWSi films, suggesting a possible mislabeling of thickness during ALD deposition, a mix up of ordering of samples during photolithography. In figure 4.21, we re-plot the average in-phase thermal resistance vs. the rearranged film thickness of TaWSi based on the assumption that the thickness of samples is indeed mislabeled. The inverse of the slope gives a value of 2.93 $Wm^{-1}K^{-1}$ which is consistent with the 80-nm HfO_2 samples, but it was calculated by changing the film thickness based on an assumption of an error. The possible way to confirm the thickness of TaWSi in these four samples is cross-sectional TEM, but due to high cost of TEM and the availability of other TaWSi samples, we decided to start measurements on new samples.

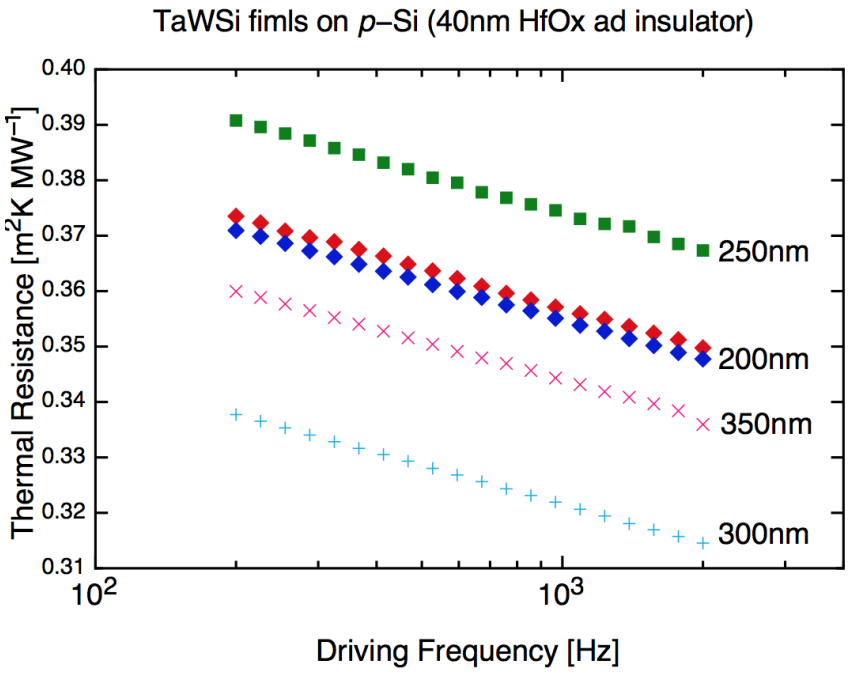

Figure 4.19: (a)Thermal resistance vs. driving frequency for a series of TaWSi films on p-type silicon. 40 nm HfOx used as insulator.

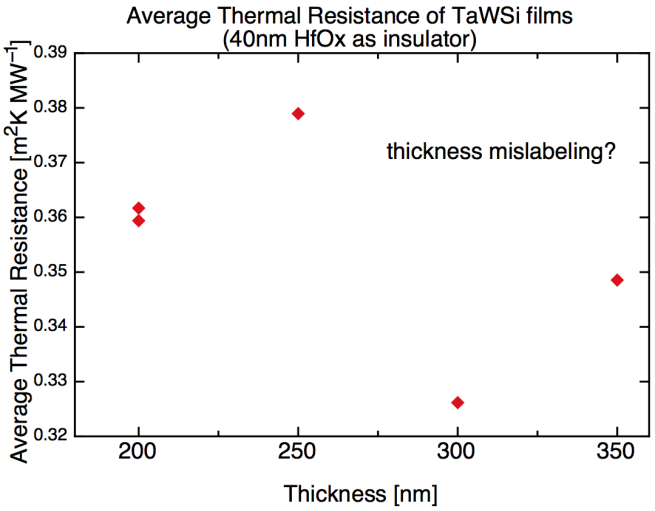

Figure 4.20: (b)Average thermal resistance vs. d_f for a series of TaWSi on p-type silicon. 40 nm HfOx used as insulator.

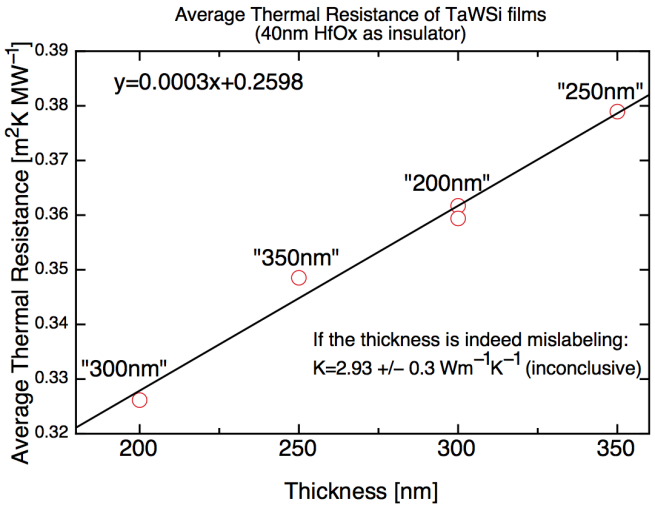

Figure 4.21: Average thermal resistance vs. d_f for a series of TaWSi on p-type silicon. 40 nm HfOx used as insulator. Based on the guess that 200 nm and 250 nm TaWSi sample were mixed with 300 nm and 350 nm respectively.

4.2.3 Thin-film TaWSi samples with 24.4 nm of HfOx insulation layer

There is a problem with these 24.4-nm HfO_2 layer samples because of breakthrough during the 3ω measurements. The results are still presented here for completeness to make a record of potential problems. 24.4 nm of HfOx is deposited on top of various thickness TaWSi films. All the results was obtained from $V_{3\omega}$ measurements and TCR measurements on 10 μm heaters.

4.2.3.1 Temperature coefficient of resistance

Figure 4.22 shows the resistance R of a heater on TaWSi samples with 24.4 nm HfOx in dependence of temperature. Linear fitting of the data points gives the slope $\frac{dR}{dT} = 0.1096$ with an fraction error of 7.4% and the resistance of heater is 48.5 Ohm.

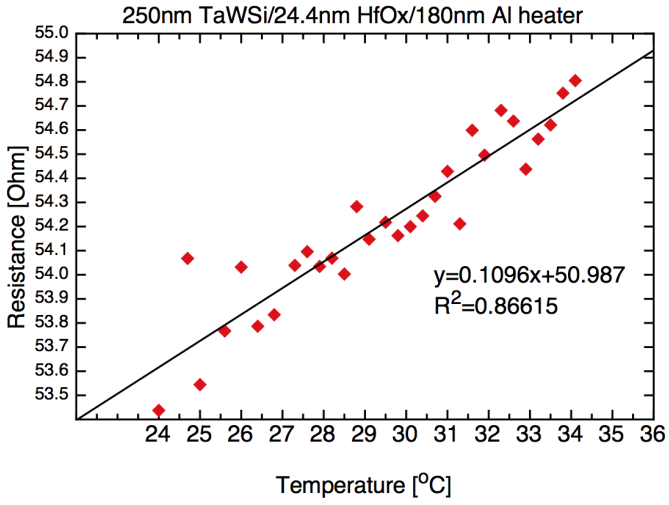

Figure 4.22: Thermal resistance vs. driving frequency for a series of TaWSi films on p-type silicon. 24.4 nm HfOx used as insulator. The heater resistance during 3ω measurement is 48.5 Ω and the temperature coefficient of resistance is 0.0023 K^{-1}.

Thus the temperature of coefficient is 0.0023 K^{-1} from the measurements. The TCR value measured here is far different from previous measurements.

4.2.3.2 3ω voltage

Figure 4.23 shows the in-phase and out-of-phase components of 3ω voltage.

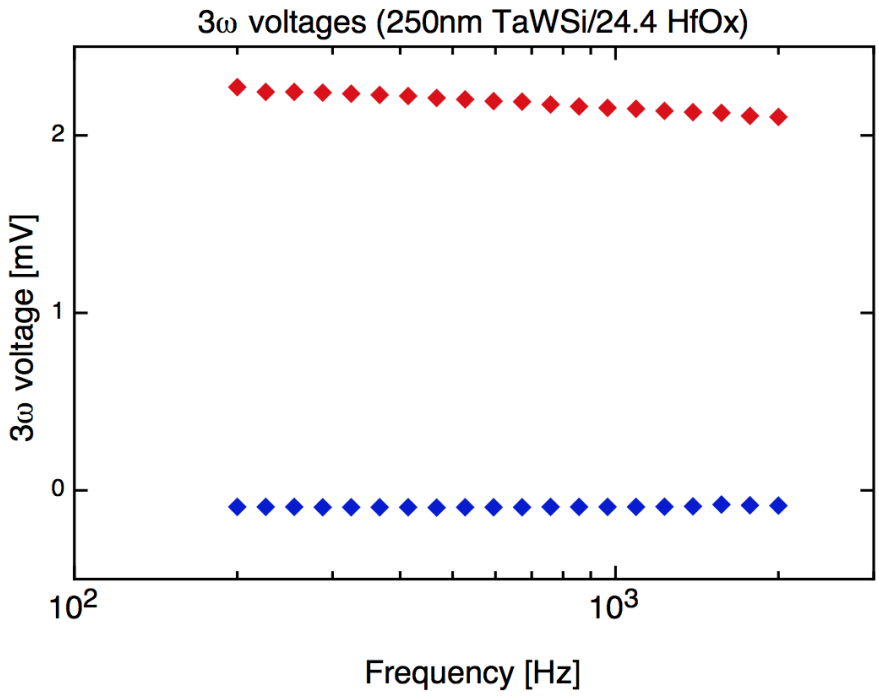

Figure 4.23: In-phase and out-of-phase components of 3ω voltage.

4.2.3.3 Thermal conductivity of TaWSi films

Figure 4.24 shows the in-phase thermal resistance vs. driving frequency for TaWSi samples with different thickness. Figure 4.25 plots the average in-phase thermal resistance vs. the film thickness of TaWSi. The measured resistance of heaters in these four samples was almost twice of measured values on previous samples for heaters with same length and same width, suggesting the thickness of aluminum

is much thinner than previous samples. A set of pogo pins were used to screw down to the voltage pads and current pads of the heaters, connecting the sample to the circuit. To ensure a good connection, pogo pins were pushed towards the samples. Because of the much thinner layer of aluminum, the pogo pins can easily beak through the aluminum layer and even the 24.4 nm HfOx layer when pushing the pogo pins for better connections. During the measurements, the resistance of heater drops a lot at the point of pushing the pogo pins towards the samples, suggesting a break through of the 24.4 nm HfOx layer by pogo pins. Most heaters was destroyed during 3ω measurements. The fact that the heater resistance is higher than the previous samples indicates the applied voltage across the heater didn't breakthrough the 24.4 nm HfOx thin film. The fact that thin layer of aluminum is easily break through by pogo pins suggests a thicker layer (at least 180 nm based on previous measurements) of aluminum is also essential.

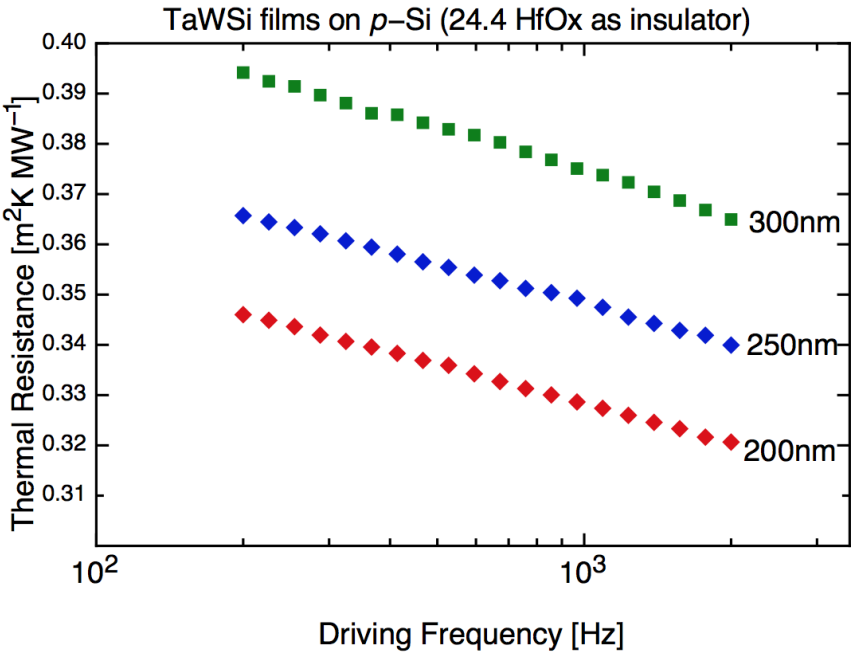

Figure 4.24: Thermal resistance vs. driving frequency for a series of HfOx films on p-type silicon.

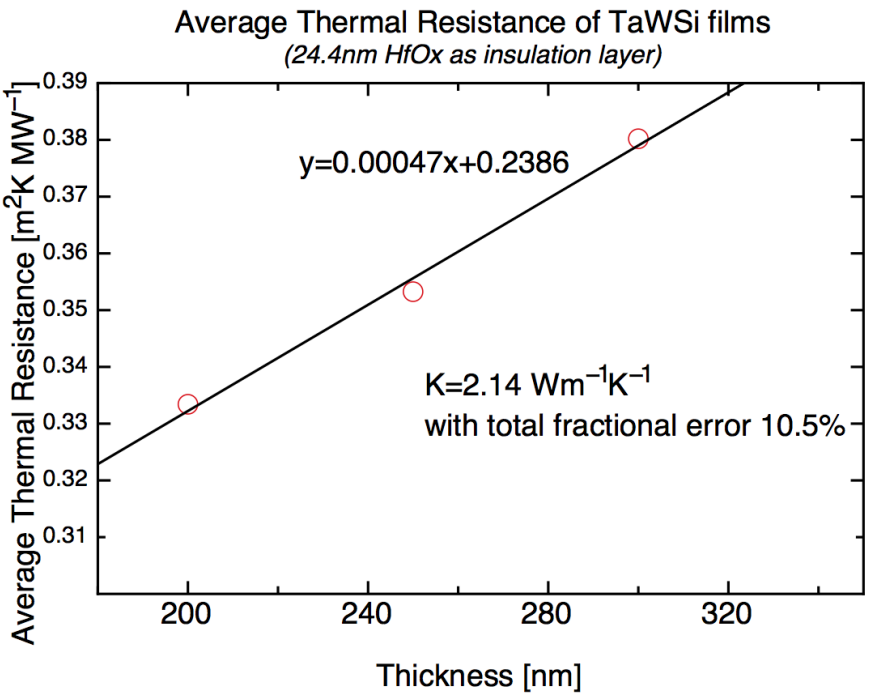

Figure 4.25: Average thermal resistance vs. d_f for a series of HfOx films on p-type silicon. Heater resistance for this set of samples is higher than previous one. Applied voltage did not breakthrough the 24.4 nm HfOx insulation layer.

From figure 4.25, the inverse slope yields the thermal conductivity of TaWSi as 2.14 $Wm^{-1}K^{-1}$ with 10.5 % total fractional error. As we can see from figure 4.22, the TCR measurement has a large fractional error than typical value. And only three different thicknesses of TaWSi were used in determining the film thermal conductivity, which makes the value we obtained here is less reliable than measurements on other sets of TaWSi samples.

4.3 Thermal conductivity measurements of silicon nitride

100 nm, 200 nm, 300 nm and 400 nm thickness of silicon nitride thin film are deposited on top of p-type silicon substrate with 100 nm thickness thermal oxide (SiO_2) at HP. The aluminum heater with a thickness of 180 nm was deposited by

thermal deposition at Owen cleanroom. The length of heaters is 1 mm while the width of heaters can be 10 μm, 15 μm, 20 μm. The heaters of this set of silicon nitride samples are produced by photolithography and aluminum wet-etching. Due to possible side etching, the width of the heater need to be measured under optical microscopy.

Figure 4.26 shows the in-phase thermal resistance vs. driving frequency for hafnium oxide samples with different thickness. Measurements was conducted on two different $10\mu m$ width heaters for each thickness. Figure 4.27 plots the average in-phase thermal resistance vs. the film thickness of HfOx. As expected, the addition of a HfOx thin film only adds a frequency independent in-phase thermal resistance increase. Based on Equation 2.47, the thermal conductivity of hafnium oxide thin film is 1.95 (± 0.29) $Wm^{-1}K^{-1}$. The intercept $\Delta R_i = 77.2 m^2 K G W^{-1}$ is the contribution of thermal resistance presented at the interface of substrate-film and film-heater.

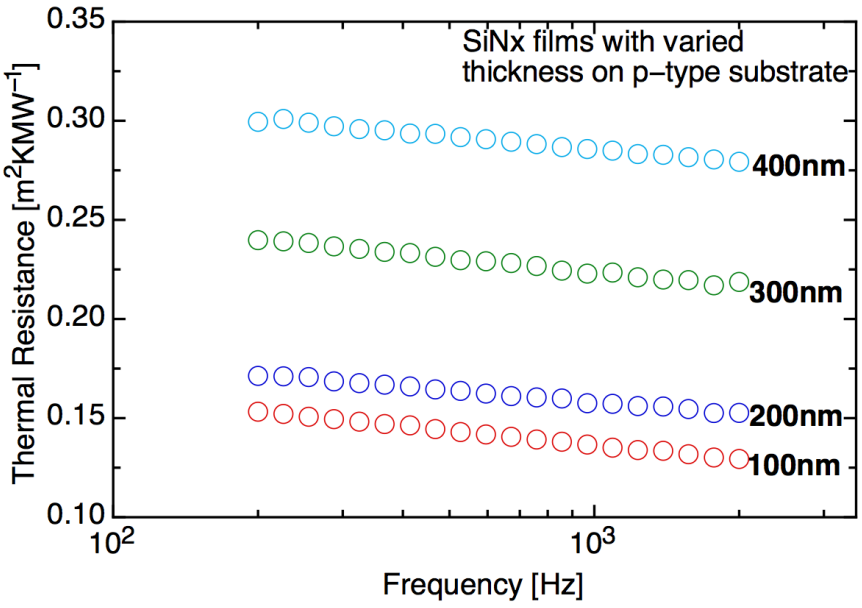

Figure 4.26: Thermal resistance vs. driving frequency for a series of SiNx films on p-type silicon.

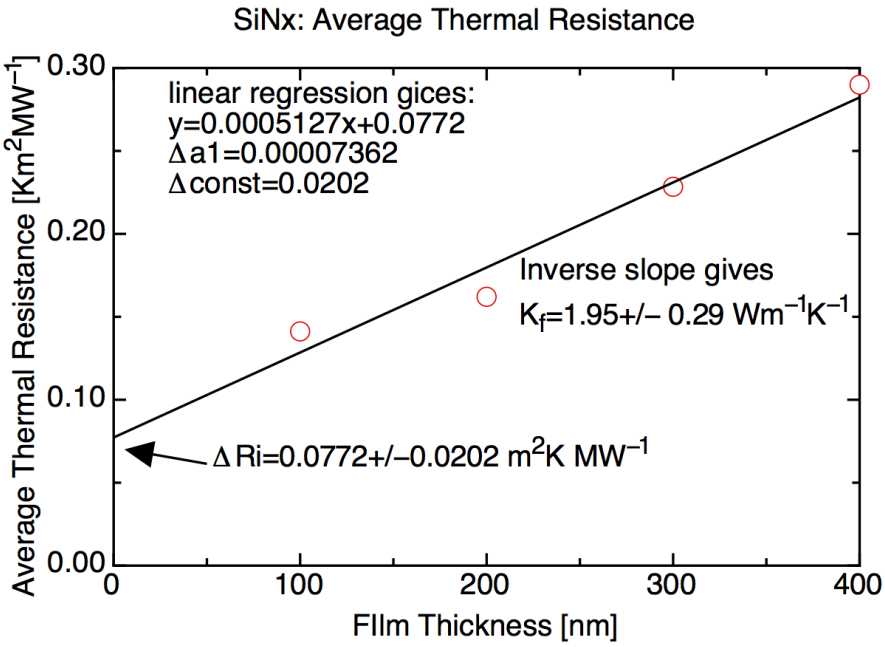

Figure 4.27: Average thermal resistance vs. d_f for a series of SiNx films on p-type silicon.

During the TCR measurements of this set of SiNx samples, the temperature keeps fluctuated and no reliable TCR measurements is achieved before all the heaters break. The TCR used in the calculation is the typical value we measured in previous samples with same heater geometry (0.00355/K). As we can see in Figure 4.27, the average thermal resistance of 100 nm and 200 nm SiNx sample is off the linear fit line. This may suggests that the thermal conductivity of SiNx depend on the film thickness and reduce the accuracy of our measurements.

Table 4.3: Results: thermal conductivity of silicon nitride films

sample	width of heater	thermal conductivity $[Wm^{-1}K^{-1}]$
SiNx	10 μm heater	1.95 $\pm$0.29

4.4 Error analysis

4.4.1 Error in width and length measurements of heaters on various samples

Figure 4.28 shows a typical example of length measurements of heaters on different samples. The length was measured by optical microscopy under 5×-amplification of the heater. The length we measured here is 1 mm, which is the same as the designed value on the mask.

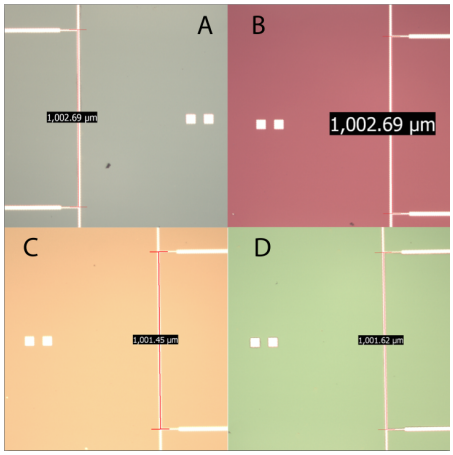

Figure 4.28: An example of length measurements. A, B, C, and D are images of heaters on four different SiNx samples (thickness of SiNX varies as 100 nm, 200 nm, 300 nm, 400 nm).

Figure 4.29 shows a typical example of width measurements of heaters on different samples. The width was measured by optical microscopy under 150×-amplification of the heater. The width we measured here is smaller than the designed value on the mask.

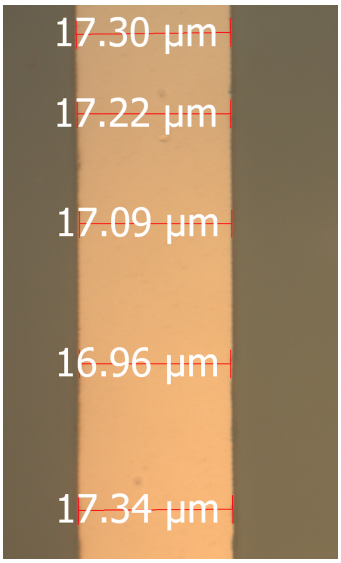

Figure 4.29: An example of width measurements to illustrate width variability.

Typically the width of a heater is smaller than the designed value on the mask. For example, the designed width of the heater in Figure 4.29 is 20 μm while the measured value is about 17 μm. Possible reasons include under-exposure and over-development during photolithography and lift-off process. During the preparation of samples, the UV lamp of the mask aligner in the cleanroom was approached the end of its lifetime. And the power distribution of that UV lamp was nonuniform. Because the exposure time and develop time can only be the same for each sample, the nonuniform distribution of UV lamp power makes the actual exposure at different places of the sample is also nonuniform. As a consequence, the actual width can be different from the designed value of the mask in a complex manner. Thus the width of heater need to be experimentally measured. We use optical microscopy with 150×-amplification to determine the width of each heater used in the 3ω measurements. For each heater, the width was measured at different locations to increase the accuracy of width measurements. The typical standard deviation of heater width is about 2 %.

The length of the heater is same as the designed value on the mask. Both the

photolithography and lift-off process will not affect the length of the heater. The width of the thin aluminum stripe that connects the voltage pads and the heater is 5 μm. The effective length of the heater may different from the length of the heater. Here we characterize the error of heater length as 1% ($= \frac{5\mu m+5\mu m}{1mm}$).

4.4.2 Error in temperature coefficient of resistance

The temperature coefficient of resistance (TCR) α is a crucial parameter for calculating the thermal conductivity. As mentioned before, the TCR of thin-film aluminum is smaller than the value for bulk aluminum. It also depends on the geometry of the heater. The length of the heater is 1 mm. The width of the heater can be $10\mu m$, $15\mu m$ and $20\mu m$. The thickness of the heater is 180 nm. The TCR of heater is more sensitive to the thickness than the width or the length of the heater. By depositing all the samples at the same time, we can minimize the difference in thickness of the heaters. Our TCR measurements suggested that the TCR of heaters with different width is almost the same as long as these heaters was deposited at the same conditions. For the TCR measurements, a small K-type-chromel-alumel thermocouple was mounted on the surface of the sample at a location close to the heater. The temperature of the heater is needed to determine the $\frac{dR}{dT}$ and further to determine the TCR. But we can only measure the temperature of a location about 2 mm away from the heater. For some TCR measurements, the distance between the heater and thermocouple is even larger. The room temperature fluctuation also affects the accuracy of the TCR measurements. To characterize $\frac{dR}{dT}$, the resistance of the heater is taken in a temperature range from 25 °C to 35 °C with 0.3 °C-steps. Multiple TCR measurements were taken on multiple heaters on different samples. The average of measured TCRs was used as the TCR to convert the $V_{3\omega}$ to the thermal resistance for all the heaters. The standard deviation is used as the systematic error of the TCR.

Chapter 5: Conclusion

We have used the 3ω method to measure the thermal conductivity of 200-350 nm amorphous TaWSi metal films deposited by DC magnetron sputtering on p-Si substrates with a 100-nm layer of thermal SiO_2. The thermal conductivity of the films is 2.4 $\pm$ 0.3 $Wm^{-1}K^{-1}$. Three sets of films were used, and the results in Table 4.2 show that our results are reproducibility when careful attention is paid to the measurement of the TCR. This result is comparable to measurements of 4.5 $Wm^{-1}K^{-1}$ reported for amorphous $Zr_{47}Cu_{31}Al_{13}Ni_9$ alloy [18].

The same 3ω technique was also used to determine the thermal conductivity of 24.4-80 nm HfO_2 layer deposited on Si/SiO_2. The thermal conductivity is 0.78 $\pm$ 0.05 $Wm^{-1}K^{-1}$, similar to a thickness dependent intrinsic thermal conductivity of 0.49 to 0.95 $Wm^{-1}K^{-1}$ reported for thin-film HfO_2 of thickness from 5.6 to 20 nm [49]. The thermal conductivity of 100-400 nm silicon nitride films deposited on Si/SiO_2 is also determined using the 3ω method. The thermal conductivity of silicon nitride is 1.95 $\pm$0.29 $Wm^{-1}K^{-1}$.

The error in the thermal conductivity measurements is dominated by the accuracy with which the temperature coefficient of resistance of the aluminum heaters used for the measurements can be determined. Each heater must be separately calibrated, making this the rate-limiting step with the largest uncertainty.

We also briefly discussed a numerical approach to simulate the oscillating temperature field based on finite element method using COMSOL. For future work, this numerical approach can be applied to interpret the data measured by the 3ω method regardless of the geometry effects of the films, heater and substrate.

Bibliography

[1] W H Wang, C Dong, and C H Shek. Bulk metallic glasses. *Materials Science and Engineering: R: Reports*, 2004.

[2] Kyuhong Lee, Kwangjun Euh, Duk-Hyun Nam, Sunghak Lee, and Nack J Kim. Wear resistance and thermal conductivity of Zr-base amorphous alloy/metal surface composites fabricated by high-energy electron beam irradiation. *Materials Science and Engineering: A*, 2007.

[3] E William Cowell III. Amorphous multi-component metals as electrode materials. Master's thesis, Electrical And Computer Engineering, Oregon State University, 2010.

[4] G D Wilk, R M Wallace, and J M Anthony. High- gate dielectrics: Current status and materials properties considerations. *J. Appl. Phys.*, 2001.

[5] Intel. http://www.intel.com/pressroom/archive/releases/2007/20071111comp.htm. Accessed June 17th, 2014.

[6] Eric Pop and Kenneth E Goodson. Thermal Phenomena in Nanoscale Transistors. *J. Electron. Packag.*, 2006.

[7] E Pop, S Sinha, and K E Goodson. Heat Generation and Transport in Nanometer-Scale Transistors. *Proc. IEEE.*

[8] Hugh O. Pierson. *Handbook of Chemical Vapor Deposition, 2nd Edition.* William Andrew, 1992.

[9] David G Cahill and Robert O Pohl. Thermal conductivity of amorphous solids above the plateau. *Phys. Rev. B*, 1987.

[10] David G Cahill. Thermal conductivity measurement from 30 to 750 K: the 3 method. *Rev. Sci. Instrum.*, 1990.

[11] David G Cahill, M Katiyar, and J R Abelson. Thermal conductivity of a-Si: H thin films. *Phys. Rev. B*, 1994.

[12] Jung Hun Kim, Albert Feldman, and Donald Novotny. Application of the three omega thermal conductivity measurement method to a film on a substrate of finite thickness. *J. Appl. Phys.*, 1999.

[13] Brandon W Olson, Samuel Graham, and Kuan Chen. A practical extension of the 3 method to multilayer structures. *Rev. Sci. Instrum.*, 2005.

[14] A Jacquot, B Lenoir, A Dauscher, M Stölzer, and J Meusel. Numerical simulation of the 3 method for measuring the thermal conductivity. *J. Appl. Phys.*, 2002.

[15] Ashok T Ramu and John E Bowers. Analysis of the "3-Omega" method for substrates and thick films of anisotropic thermal conductivity. *J. Appl. Phys.*, 2012.

[16] River A Wiedle, Mark Warner, Janet Tate, Paul N Plassmeyer, and Catherine J Page. Thermal conductivity of amorphous thin-film Al–P–O on silicon. *Thin Solid Films*, 2013.

[17] G Andrew Antonelli, Bernard Perrin, Brian C Daly, and David G Cahill. Characterization of Mechanical and Thermal Properties Using Ultrafast Optical Metrology. *MRS Bulletin*, 2006.

[18] Nitin C Shukla, Hao-Hsiang Liao, Jeremiah T Abiade, Fengxiao Liu, Peter K Liaw, and Scott T Huxtable. Thermal conductivity and interface thermal conductance of amorphous and crystalline $Zr_{47}Cu_{31}Al_{13}Ni_9$ alloys with a Y_2O_3 coating. *Appl. Phys. Lett.*, 2009.

[19] Yee Kan Koh, Suzanne L Singer, Woochul Kim, Joshua M O Zide, Hong Lu, David G Cahill, Arun Majumdar, and Arthur C Gossard. Comparison of the 3 method and time-domain thermoreflectance for measurements of the cross-plane thermal conductivity of epitaxial semiconductors. *J. Appl. Phys.*, 2009.

[20] David Cahill. http://users.mrl.illinois.edu/cahill/3omega10.pdf. accessed may 15th, 2014.

[21] River Alan Wiedle. Thermal conductivity measurements of amorphous thin films on silicon via the 3ω method, 2013.

[22] Nicola Schmidt. Measurement of the thermal conductivity of thin films by the 3-ω method, 2012.

[23] Hans J. Weber George B. Arfken and Frank E. Harris. *Mathematical Methods for Physicists, Seventh Edition*. Academic Press, 2012.

[24] Irene A. Stegun Milton Abramowitz. *Handbook of Mathematical Functions, ninth edition*. Courier Dover Publications, 1972.

[25] Farshad Faghani. Thermal conductivity measurement of PEDOT: PSS by 3-omega technique. 2010.

[26] A J Griffin, F R Brotzen, and P J Loos. The effective transverse thermal conductivity of amorphous Si3N4 thin films. *J. Appl. Phys.*, 1994.

[27] A Jacquot, B Lenoir, A Dauscher, M Stölzer, and J Meusel. Numerical simulation of the 3 method for measuring the thermal conductivity. *J. Appl. Phys.*, 2002.

[28] C E Raudzis, F Schatz, and D Wharam. Extending the 3 method for thin-film analysis to high frequencies. *J. Appl. Phys.*, 2003.

[29] J L Battaglia, C Wiemer, and M Fanciulli. An accurate low-frequency model for the 3 method. *J. Appl. Phys.*, 2007.

[30] Purdue University. Thermophysical Properties Research Center. *Thermophysical properties of matter: the TPRC data series; a comprehensive compilation of data*. IFI/Plenum, 1979.

[31] Mary P. Lord Arthur M. James. *MacMillan's Chemical and Physical Data*. Macmillan, 1992.

[32] http://www-pub.iaea.org/mtcd/publications/pdf/te_1496_web.pdf. accessed june 4th, 2014.

[33] P Esquinazi and F de La Cruz. Phonon thermal conductivity limited by electron scattering in amorphous Zr 70 Cu 30. *Phys. Rev. B*, 1983.

[34] Patrick E Hopkins, Manli Ding, and Joseph Poon. Contributions of electron and phonon transport to the thermal conductivity of GdFeCo and TbFeCo amorphous rare-earth transition-metal alloys. *J. Appl. Phys.*, 2012.

[35] David G Cahill, Susan K Watson, and Robert O Pohl. Lower limit to the thermal conductivity of disordered crystals. *Phys. Rev. B*, 1992.

[36] B Zink, R Pietri, and F Hellman. Thermal Conductivity and Specific Heat of Thin-Film Amorphous Silicon. *Phys. Rev. Lett.*, 2006.

[37] Brian C Daly, George A Antonelli, Humphrey J Maris, Wayne K Ford, Larry Wong, and Ebrahim Andideh. Measurements of the thermal conductivity of amorphous materials with low dielectric constants. *Physica B: Condensed Matter*, 2002.

[38] Norman Henry March William Jones. *Theoretical Solid State Physics*. Courier Dover Publications, 1985.

[39] Charles Kittel. *Introduction to Solid State Physics*. Wiley, 2005.

[40] Paothep Pichanusakorn and Prabhakar Bandaru. Nanostructured thermoelectrics. *Materials Science and Engineering: R: Reports*, 2010.

[41] A J Minnich, M S Dresselhaus, Z F Ren, and G Chen. Bulk nanostructured thermoelectric materials: current research and future prospects. *Energy Environ. Sci.*, 2009.

[42] R C Zeller and R O Pohl. Thermal conductivity and specific heat of noncrystalline solids. *Phys. Rev. B*, 1971.

[43] c. M. Varma P. w. Anderson, B. I. Halperin. Anomalous low-temperature thermal properties of glasses and spin glasses. *Philosophical Magazine*, 1972.

[44] P W ANDERSON, B I HALPERIN, and C M VARMA. Anomalous low-temperature thermal properties of glasses and spin glasses. *PHILOSOPHICAL MAGAZINE*, 1972.

[45] Fred Lacy. Investigating thin films for use as temperature sensors. 2007.

[46] http://www.webelements.com/periodicity/thermal_conductivity/. accessed may 15th, 2014.

[47] Michiaki Yamasaki, Shinya Kagao, and Yoshihito Kawamura. Thermal diffusivity and conductivity of Zr55Al10Ni5Cu30 bulk metallic glass. *Scripta Materialia*, 2005.

[48] D M Rowe and C M Bhandari. Preparation and thermal conductivity of doped semiconductors. *Progress in crystal growth and characterization*, 1986.

[49] Matthew A Panzer, Michael Shandalov, J A Rowlette, Yasuhiro Oshima, Yi Wei Chen, Paul C McIntyre, and Kenneth E Goodson. Thermal Properties of Ultrathin Hafnium Oxide Gate Dielectric Films. *IEEE Electron Device Lett.*, 2009.